

Anterior Segment of Eye: Imaging and Image Analysis

D Vikram Goud

A Thesis Submitted to
Indian Institute of Technology Hyderabad
In Partial Fulfillment of the Requirements for
The Degree of Master of Technology



भारतीय प्रौद्योगिकी संस्थान हैदराबाद
Indian Institute of Technology Hyderabad

Department of Electrical Engineering

June 2018

Declaration

I declare that this written submission represents my ideas in my own words, and where ideas or words of others have been included, I have adequately cited and referenced the original sources. I also declare that I have adhered to all principles of academic honesty and integrity and have not misrepresented or fabricated or falsified any idea/data/fact/source in my submission. I understand that any violation of the above will be a cause for disciplinary action by the Institute and can also evoke penal action from the sources that have thus not been properly cited, or from whom proper permission has not been taken when needed.

D. Vikram Goud.

(Signature)

D. Vikram Goud.

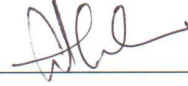
(D Vikram Goud)

EE15MTECH11022.

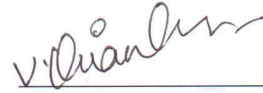
(Roll No. EE15MTECH11022)

Approval Sheet


This thesis entitled Anterior Segment of Eye - Imaging and Image analysis by D VIKRAM GOUD is approved for the degree of Master of Technology from IIT Hyderabad.



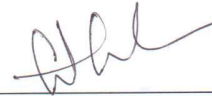
(Dr. Sumohana Channappayya) Examiner
Department of Electrical Engineering
Indian Institute of Technology Hyderabad



(Dr. Kiran Kumar Vupparaboina) Examiner
Srujana Innovation Center
L. V. Prasad Eye Institute Hyderabad



(Dr. Soumya Jana) Adviser
Department of Electrical Engineering
Indian Institute of Technology Hyderabad



(Dr. Sumohana Channappayya) Chairman
Department of Electrical Engineering
Indian Institute of Technology Hyderabad

Acknowledgements

I consider myself fortunate to get admitted into the masters program at IIT Hyderabad, and even more fortunate to have Prof. Soumya Jana as my advisor. I will always be indebted to him for his invaluable guidance. Most of my research was carried in association with Kiran Kumar Vupparaboina, our lab's first PhD student. No word can fully convey my sincere gratitude and respect for him. I also thank L V Prasad Eye Institute Hyderabad for funding me and providing a great environment enabling exchange of ideas with clinicians, unfettered access to medical data and other resources.

It was pleasure to spend long hours in the lab, especially having technical discussions and fun activities. I would like to thank my labmates Roopak R. Tamboli, B Sandeep Chandra, Anand Kakarla, M Shanmukh Reddy, A Srinivas, Mohammed Nasar, Sathish Ande, Vishwanath Rathod, M V Pavan, Adarsh, Kishore, Nanda Sailaja, Loke Sankrandan, Ranjith and Rajashekar for helping me in various aspects. I am thankful to Yeshwanth Manchuri, my roommate, for being a good friend and sharing many good moments. I also extend my thanks to 2015 M.Tech Electrical batch for creating cherishable moments and supporting me directly or indirectly.

Above all I would like to thank my parents and other family members for constantly supporting me in my not-always-smoothsailing endeavors.

Dedication

I would like to dedicate my thesis to my family and
Immersive Multimedia Telepresence Lab.

Abstract

Anterior segment of eye mainly consists of Cornea, Anterior Chamber, Iris and Lens. The anatomy of these optical structures will determine the quality of vision and nature of eye. So imaging and image analysis can be used in the diagnosis of the eye. In this thesis three problems are addressed one on imaging system design and another two on image processing.

In the first problem, Design of continuous zoom slit lamp camera, an imaging system with continuous zoom is designed with constraint to be compatible with discrete zoom system. From paraxial analysis it is found that optimal choice of the lenses will improve the magnification range of the continuous system. By using the optical simulation software (Optics studio, Zemax), complete real lens model is designed and the resultant system is having spot size within the diffraction limit, distortion is less than 1% and very less aberration values throughout the zoom range.

In the second problem, Automated 3D modeling and quantification of cornea graft detachment post DSAEK based on AS-OCT images, an image processing methodology is developed to detect the detachment region between donor lenticule and host Cornea, detect nature of detachment (communicative or non-communicative) and form complete 3D of the Cornea using AS-OCT images of after DSAEK operation. Statistical analysis are performed to check the accuracy of proposed methodology, it is found that the algorithmic values are closely following the manual values.

In the third problem, Automated anterior chamber depth detection using Pentacam camera images, an image processing methodology is developed to detect the depth of the anterior chamber not only at central location but also at different locations. In order to aid the complete 3D anterior chamber and 3D depth profile formation in future, Pentacam images are first segmented and depth values are calculated.

Contents

Declaration	ii
Approval Sheet	iii
Acknowledgements	iv
Abstract	vi
1 Introduction	1
2 Zoom Slit Lamp Design	3
2.1 Introduction	3
2.2 Problem statement	4
2.3 Methods	5
2.4 Results	11
2.5 Discussion and future work	12
3 Corneal OCT Analytics	22
3.1 Introduction	22
3.2 Methods	26
3.2.1 Data acquisition	26
3.2.2 Proposed Methodology	26
3.2.3 Reference Performance: Inter-Observer Repeatability	32
3.2.4 Algorithmic Performance Criteria	34
3.3 Results	35
3.3.1 Thickness estimates of recipient cornea and donor lenticule	37
3.3.2 Volume estimates and overall thickness profile	39
3.4 Discussion	41
3.A Yen's Thresholding	42
3.B Circle fitting	43
3.C Hessian matrix analysis	44
3.D Max Entropy Criteria Thresholding	44

4	Anterior Chamber Depth Analysis	46
4.1	Introduction	46
4.2	Methods	48
4.2.1	Data acquisition	48
4.2.2	Proposed Methodology	49
4.3	Results	52
4.4	Conclusion and Future Work	53
5	Conclusion and Future Work	55
	References	57

List of Figures

2.1	Detailed illustration of Kepler’s telescope formation : (a) Converging lens is focusing parallel rays at focus, (b) when point source is at the focal length of a lens and (c) Kepler’s telescope as the combination two converging lenses.	5
2.2	Detailed illustration of Galilean’s telescope formation : (a) Diverging lens is focusing parallel rays at focus (when elongated), (b) when point source is at the focal length of a lens and (c) Galilean’s telescope as the combination converging lens and diverging lens.	6
2.3	Bio microscope: (a) Bio microscope of the Slit lamp camera (red box) and (b) Ray diagram diagram of Bio microscope.	7
2.4	Discrete zoom system :(a) Rotation drum in slit lamp (red box), (b) Ray diagram diagram of Bio microscope with afocal system introduced by rotation drum, (c) Rotation drum and (b) Galilean system with tele-centric optical path.	7
2.5	Proposed 3 lens afocal system.	9
2.6	Moment of the lenses in afocal system.	12
2.7	Variation of the magnification of Images with zoom.	13
2.8	The variation d_1 , d_2 and total system length as a function of magnitude.	14
2.9	Moment of the lenses in afocal real lens system.	14
2.10	Variation of the magnification of Images with zoom.	15
2.11	The variation d_1 , d_2 and total system length as a function of magnitude.	16
2.12	The variation d_1 , d_2 and total system length as a function of magnitude.	16
2.13	Moment of the lenses with zoom.	17
2.14	Variation of the magnification of Images with zoom.	18
2.15	Variation of the grid distortion of Images with zoom.	19
2.16	Variation of the seidel diagrams of Images with zoom.	20
2.17	Variation of the spot diagram of Images with zoom.	21

3.1	(a)–(d). Typical AS-OCT radial scans of a subject taken with 45° separation post DSAEK. (e) Graphical representation of locations of four radial scans captured.	25
3.2	Schematic of proposed methodology.	27
3.3	Graphical representation of proposed methodology: (a) AS-OCT image, (b) Yen’s thresholding, (c) Detected cornea outer boundary, (d) Detected cornea inner boundary (e) Vesselness-filtered estimate in ROI, (f) Maximum entropy criteria thresholding on vesselness-filtered estimate, (g) Initial estimate of the detachment by extracting biggest connected component (h) Contour of the initial estimate, (i) Smoothened initial estimate, (j) Initial estimate overlaid on the image, (k) Central line passing through the detachment, and (l) Final estimate of the detachment after detecting connected components along the central line.	29
3.4	Detailed illustration of cornea outer boundary detection: (a) AS-OCT image, (b) Initial estimate obtained by reading first significant intensity gradient (c) Estimate after performing morphological open-close operation and (d) Final estimate after circle fitting.	30
3.5	Detailed illustration of cornea outer boundary detection: (a) OCT image, (b) Initial estimate obtained by reading first significant intensity gradient from bottom and (c) Final estimate after removing the spurious dip at the center.	30
3.6	(a) OCT image; (b) Extraction of recipient cornea and donor lenticule based on central axis (green line) of detachment; and (c) dividing OCT image into two halves based central axis (yellow dotted line) to facilitate 3D mapping.	31
3.7	Interpolation to obtain intermediated scans: (a)–(c) Intermediate 100 points (green dotted line) on the lines (blue dotted lines) obtained by interpolation of 100 equidistant points chosen on upper and lower boundaries of detachment region extracted from 0° and 45° scans (red regions); (d)–(f) Different views of four interpolated regions (green contour) obtained between adjacent 45° segments (red) extracted; (g)–(i) Different views of eight interpolated regions (green contour) obtained between adjacent 45° segments (red) extracted.	33

3.8	3D visualization: (a) Recipient cornea; (b) Detachment region, (c) Donor lenticule, (d) Detachment and donor lenticule regions together, (e) Detachment and recipient regions together, (f) Recipient and lenticule regions together.	35
3.9	Qualitative comparison of segmentation of detachment achieved by proposed method (yellow) and manual methods (maroon and orange) on radial AS-OCT scans of five representative subjects.	36
3.10	Normalized difference in DC between proposed (DC^{auto}) and manual (DC^{inter}) methods.	37
3.11	Thickness estimates for recipient cornea (green) and donor lenticule (yellow) at central and peripheral locations.	37
3.12	Volume estimates of detachment obtained by proposed and manual methods (manual method here indicates average of volumes estimate by all four observer delineations).	39
3.13	Thickness profile of the detachment for the representative images shown in Fig. 3.9. Note: Scale is shown in μm	40
4.1	Schematic of proposed methodology.	48
4.2	Preprocessing: (a) Pentacam anterior chamber image, (b) Log linear transformed image, (c) Adaptive thresholding image, and (d) Enhanced image.	49
4.3	Cornea extraction : (a) Enhanced image, (b) Largest connected component, (c) Cornea outer boundary, (d) Dilate Cornea region, (e) Cornea region of Log linear transform image, and (f) Cornea inner boundary.	50
4.4	Lens extraction : (a) Image close operation Enhanced image, (b) Largest connected component, (c) The region below Cornea, (d) Image open operation, (e) component touching the vertical line, and (f) Lens top edge labeled image.	52
4.5	Iris extraction : (a) The region below Cornea, (b) After removing the Lens, (c) Enhanced image region, (d) After removing parallel and tiny components, (e) Canny edge detection, and (f) Iris labeled image.	53
4.6	Segmentation result.	53
4.7	Depth labeled image.	54
4.8	Anterior chamber depth values and comparison of average with reference.	54

List of Tables

2.1	Existing discrete zoom system parameters.	8
3.1	Intra- vs Inter-observer repeatability. Notation: M^A – Manual segmentations by observer A, M^B – Manual segmentations by observer B, M – Manual reference (average).	36
3.2	Statistical analysis based on Dice coefficient.	37
3.3	Thickness estimates of recipient cornea and donor lenticule obtained algorithmically and manually (average of four manual estimates). Notation: SD–Standard deviation.	38
3.4	Comparison of volume estimates of detachment region obtained by the proposed and manual methods. Notation: M^A – Average of two manual segmentations performed by observer A; M^B – Average of two manual segmentations performed by observer B; M –Average of M^A and M^B	39

Chapter 1

Introduction

Anterior segment of eye: imaging and image analysis, is a study of techniques used for the diagnosis of the eye. In particular, in this thesis we restrict ourselves to anterior segment of human eye. Considering the anatomy of human eye, the entire eye can be split into two halves: anterior segment and posterior segment. Anterior segment of eye mainly consists of Cornea, Anterior chamber, Iris and Lens. The shape, structure and relative position of these optical structures play a vital role in the quality of vision and overall health of the eye. Accidents, diseases and perhaps surgeries may change these optical structures. So imaging and image analysis can play an important role in their diagnosis. In this thesis, the following problem are addressed,

Imaging :-

1. Design of continuous zoom slit lamp camera

Image analysis : -

2. Automated 3D modeling and quantification of cornea graft detachment post DSAEK based on AS-OCT images
3. Automated anterior chamber depth detection using Pentacam camera images

The first problem, "Design of continuous zoom slit lamp camera", concentrates on designing a continuous zoom slit lamp camera, in contrast to well-established slit lamp cameras having only discrete zoom. The continuous zoom design, not only aid the clinicians in choosing the region of interest precisely but also overcomes the chin rest positioning with the addition of auto focus objective lens. Towards this, we make an attempt to design the complete bio microscope using optical simulation software, Zemax and compare the optical parameters: spot radius and aberration plots.

The second problem, "Automated 3D modeling and quantification of cornea graft detachment post DSAEK based on AS-OCT images.", aims to identify detachment location in the Cornea, nature of detachment (communicative or non-communicative)

in post DSAEK surgery and generating complete 3D profile of donor, host and detachments. The progress of movement in donor graft away from the host Cornea helps clinicians for better diagnosis. The images of cornea are acquired using AS-OCT imaging system. The algorithmic results will be compared with the manual results using statistical analysis.

The third problem, "Automated anterior chamber depth detection using Pentacam camera images.", is an image processing problem. Rather than calculating the depth at central location of the Lens using special equipments like Lasers, in this study the anterior chamber depth will be calculated at different locations by using only the images of Pentacam camera. In our method we propose to calculate the depth at different locations and also form a complete 3D of anterior chamber with corresponding depth profile. To meet these requirements, all the parts of the eye will be segmented separately and then depth calculations will be performed.

Chapter 2

Zoom Slit Lamp Design

The slit lamp camera, well-established ophthalmologic device, mainly used for the analysis of the anterior segment of eye. Most of the slit lamp cameras available in the market are having discrete zoom (step wise). Having continuous zoom over discrete will always helpful. In the long run, by adding the auto focus lens to the continuous zoom slit lamp camera, we can overcome the requirement of keeping the head in chin rest chamber. Designing a continuous zoom system without losing the image quality and also to be compatible with the well-established slit lamp model is the main aim of this study. By starting with paraxial modeling of afocal system, complete bio microscope is designed in this study using the optical simulation software zemax .

2.1 Introduction

The slit lamp camera, well established ophthalmologic device, mainly used for the analysis of the anterior segment of eye. It is an instrument consisting of a high-intensity light source that can be focused to shine a thin sheet of light on the eye. It is used in conjunction with a bio microscope for the observation of the eye through it. The slit lamp camera is used to examine the anterior segment of eye i.e. Cornea, Iris, Lens and Anterior chamber. It is also used for extra ocular analysis i.e. observation of eye lids and Caruncle. It can be extended for posterior segment and iridocorneal angle observations. The electronic documentation of the patient's condition is increasing its importance. So the present slit lamp cameras are interface with computers for the electronic documentation.

The main aim of this study is to design a continuous zoom slit lamp camera. The main motivation is that the observer can select the region of his interest without any compromise. And also in future, by adding the auto focus lens, can overcome the

requirement of chin rest chamber i.e. the patient need not to bend his head and keep his head in the chin rest chamber.

A zoom system is generally considered to consist of three parts: the focusing, zooming and fixed parts. The focusing part is placed in front of the zooming part to adjust the object distance. The zooming part is literally used for zooming and the fixed rear part serves to control the focal length or magnification and reduce the aberrations of the whole system. Several of the published papers [1–5] concerning zoom have concentrated on the first-order zoom design. Generally zoom systems are considered to be focal in nature i.e. having the non infinity focal length values. The zoom system are expressed in terms of their focal length range or magnification range. An afocal zoom system [6, 7] is nothing but a zoom system which is having infinity focal length through out it's zoom range. Generally an afocal zoom system is expressed in terms of it's magnification range. An afocal zoom is simply a focal zoom system without the fixed rare part.

In this study, a different approach is used to design a continuous zoom slit lamp camera, i.e. rather than designing the complete imaging model (bio microscope), the idea is to replace the circular drum, which is accounting for the discrete zoom, with a continuously varying zoom lens model. So essentially need to design afocal system with continuously varying magnification, which is compatible with the existing model. The report starts with a paraxial modeling of afocal system and then converted into real lens model. For designing the real system, each paraxial lens is replaced with a triplet as motivated by cookes triplet design (The Cooke triplet lens was first invented in 1893 (see British Patent Nos. 15,107 and 22,607, and U.S. Patent Nos. 540,122 and 568,052)) because triplet will have enough number of parameters to overcome all the 3rd order aberrations [8]. The same procedure is applied for the complete imaging system design. Optical simulating software Zemax Optics studio (version 15.5) and matlab are used for this study.

The rest of the chapter is organized as follows. Section 2 presents the problem statement, Section 3 details the proposed methodology. Subsequently, Section 4 presents experimental results. Finally, Section 5 concludes the work with discussion.

2.2 Problem statement

Traditional slit lamp cameras are having discrete zoom (stepwise) optical system. Designing an alternative continuous zoom system without losing the image quality and also to be compatible with the well-established slit lamp model.

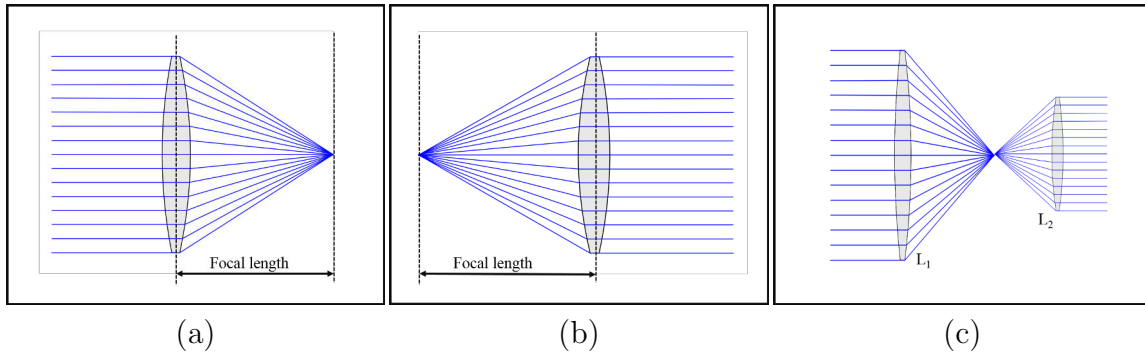


Figure 2.1: Detailed illustration of Kepler's telescope formation : (a) Converging lens is focusing parallel rays at focus, (b) when point source is at the focal length of a lens and (c) Kepler's telescope as the combination two converging lenses.

2.3 Methods

In order design a continuous zoom slit lamp camera or any other optical device, there exists a particular procedure to meet the requirements in an efficient way. The procedure can be divided into the following steps,

1. Parameter extraction
2. Parxial design and analysis
3. Real lens design and analysis

In order to understand the parameters and lens design procedure, it is better to know about basics of optics. Here we are presenting the basic information to understand this project, it is advised to know more about optics [9–11]. Lens is an optical device which works the principle of refraction. Lenses are mainly classified into two types, one is converging lens and other is diverging lens. When collimated light (parallel rays of light) enters into a converging lens, the light will get refracted and converge at the location, which is know as focal point and the distance from lens to that point is known as focal length(Fig. 2.1(a)). The reverse should also hold good, i.e. when diverging light fall on a lens from a point source which is at focal length distance from the lens, then the light ray will be collimated after refraction(Fig. 2.1(b)). On the other hand, the diverging lens will diverge the rays after refracting through the lens, but when elongate these diverging rays in the opposite direction, they will converge at a point which is known as the focus(Fig. 2.2(a-b)).

Both converging and diverging lenses are considered as focal systems, as they have a focus at a finite distance. Whenever a system doesnt have any focus, such system is known as afocal system. The focal length is considered as infinity and both the input and output rays are collimated in nature. It can be achieved by placing a lens

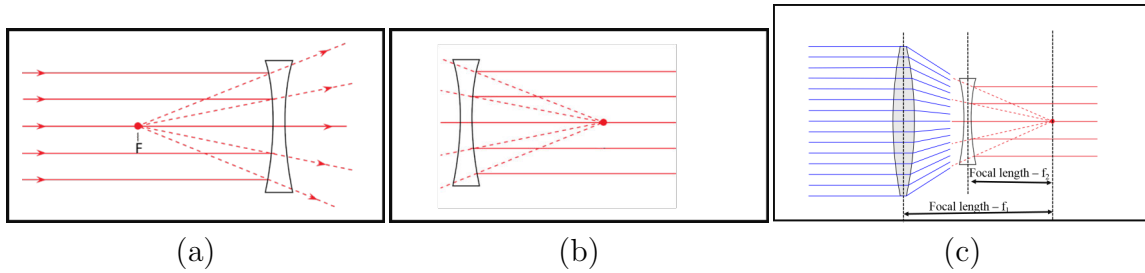


Figure 2.2: Detailed illustration of Galilean's telescope formation : (a) Diverging lens is focusing parallel rays at focus (when elongated), (b) when point source is at the focal length of a lens and (c) Galilean's telescope as the combination converging lens and diverging lens.

at focal length distance from the focus of an another lens. When both the lenses are converging lenses (Fig. 2.1(c)), which is well known as an Kepler telescope. Later by placing the diverging lens and converging lens at a separation of sum of their focal lengths, Galileo invented non inverting telescope(Fig. 2.2(c)).

For deciding the specifications, we are using the Carl Zeiss company discrete zoom slit lamp camera (SL 120 Slit Lamp) as reference. The main reason for choosing this over few continuous zoom slitlamp cameras is that as discrete system will always have better performance over the continuous once because the number of variables are more in discrete system over the continuous system. Reference slit lamp camera is show in the figure 2.3(a). Here we are going to concentrate on the bio microscope(highlighted in red box) and equivalent ray diagram is also shown in figure 2.3(b). If we consider the bio microscope from right to left, first part is objective lens, generally we place the patient eye at the focal plane of the objective lens which means the working distance of the system is the focal length of the objective lens. This objective lens will collimate the rays form the object(patient eye). Then these rays will pass though the afocal system, i.e. which will allow collimated rays and sends out collimated ray by changing their magnification. The final part is the eyepiece, which will focus the rays on the retina of the observer.

Here the variation of the magnification is due to the cylindrical drum(Fig. 2.4(a-d))(Fig. 2.3 and Fig. 2.4 are taken from user manual of the device SL 120 Slit Lamp, Carl Zeiss.), by rotating which we are changing the magnification. By rotating the drum, we are essentially changing the afocal system present in the bio microscope. The Galilean system with telecentric optical path is used as the drum like structure. In this model, two gelian telescopes are there which are arranged in a telecentric fashion in a drum like structure. When the drum is rotated one among them will

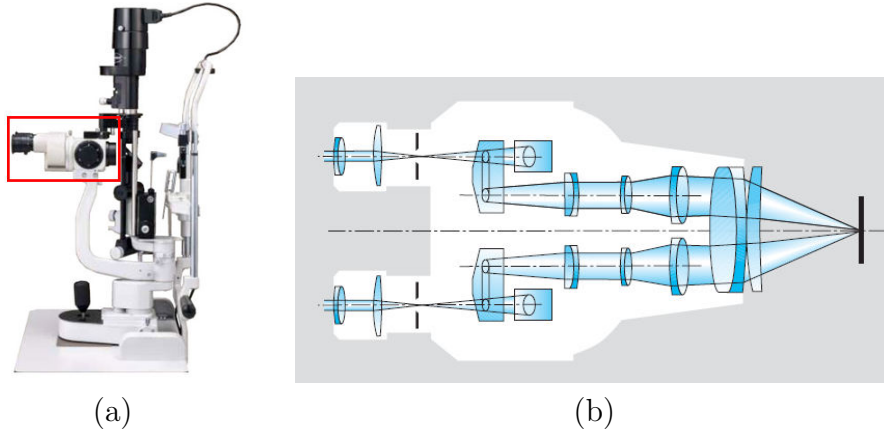


Figure 2.3: Bio microscope: (a) Bio microscope of the Slit lamp camera (red box) and (b) Ray diagram diagram of Bio microscope.

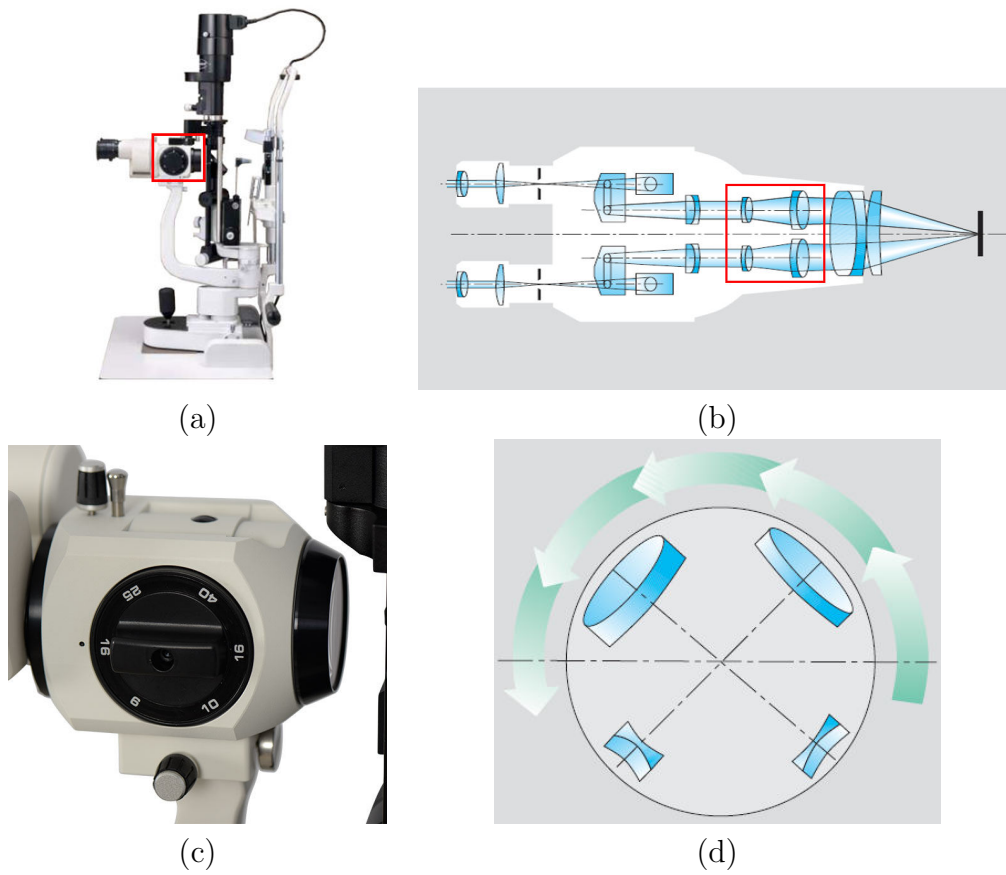


Figure 2.4: Discrete zoom system : (a) Rotation drum in slit lamp (red box), (b) Ray diagram diagram of Bio microscope with afocal system introduced by rotation drum, (c) Rotation drum and (d) Galilean system with tele-centric optical path.

come into the optical path. Let M_{sys} be the magnification of the system without any

	Mode	Afocal system magnification	Total magnification
Without afocal system		1	16
Afocal system 1	Forward	1.5	25
	Reverse	0.6	10
Afocal system 2	Forward	2.5	40
	Reverse	0.4	6

Table 2.1: Existing discrete zoom system parameters.

afocal lens in the optical path. Let M_1 be the magnification of the afocal system, then the resultant magnification of the entire system is $M_{sys} * M_1$. By rotation the drum 180 degrees, the afocal system with magnification M will become afocal system with magnification $1/M$.

So two afocal systems in the cylindrical drum will results in 5 magnifications (front 2, reverse 2 and without any system in the optical path). The magnification values of the given system are shown in table 2.1 . The minimum magnification of the afocal system is 0.4 and the maximum of that is 2.5. the total afocal system length is 80mm and diameter of the opening of the rotating drum is 30mm. The targeted continuous zoom system should have the minimum magnification range of 0.4 - 2.5 mm with an opening diameter of 30mm and maximum total system length of 80mm.

The magnification(M) of an afocal system is given by

$$\text{Magnification}(M) = -1X \frac{\text{focal length of objective}}{\text{focal length of eyepiece}}. \quad (2.1)$$

The separation distance between lenses must be equal to the sum of focal lengths of objective lens and the eyepiece. In case of Keplerian model, both the lenses are having positive focal lengths where as in case of Galilean type system, one is having positive focal length and the other is having the negative focal length. So the total length of the system is less incase of Galilean system. So we are using the Galilean type afocal system as the base for the formulation of continuous zoom system. The magnification of the Galilean type system can be varied by either varying the focal length of objective lens or the eyepiece.

$$M_{variable} = -1X \frac{(\text{focal length of objective})_{variable}}{(\text{focal length of eyepiece})}. \quad (2.2)$$

Or

$$M_{variable} = -1X \frac{(\text{focal length of objective})}{(\text{focal length of eyepiece})_{variable}}. \quad (2.3)$$

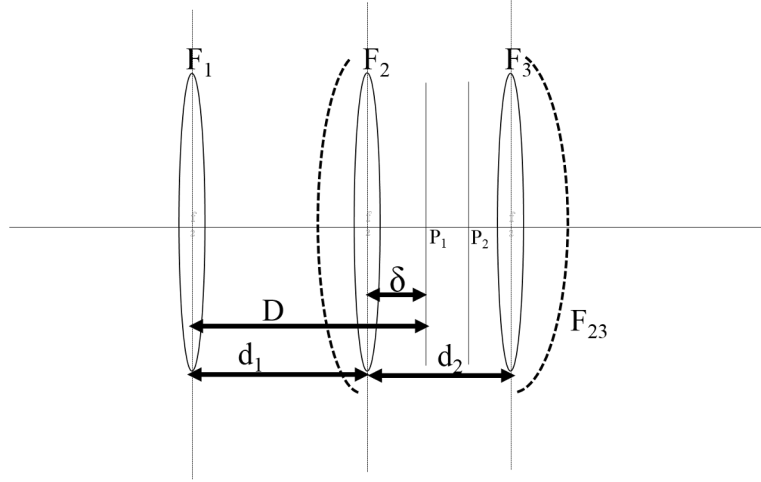


Figure 2.5: Proposed 3 lens afocal system.

The focal length of any lens can be varied by formulating the lens as the combination of lenses with separation, by varying the separation between the fixed focal length lenses, the effective focal length can be varied.

Let F_1 , F_2 and F_3 are the focal lengths of the 3 lenses and their respective powers are K_1 , K_2 and K_3 (lens power is the reciprocal of it's focal length). Let d_1 be the distance between the lens - 1 and the lens - 2 and d_2 be the separation of between system lens - 2 and lens - 3. The same arrangement of the lenses is shown in the figure 2.5. Assume that second and third lens are forming a single lens component (K_{23}), whose power is given by

$$K_{23} = K_2 + K_3 - K_2 K_3 d_2. \quad (2.4)$$

The magnification (M) of such system is given by

$$M = \frac{(Image\ height)}{(Objective\ height)} = -\frac{F_1}{F_{23}}. \quad (2.5)$$

The afocal condition need to be maintained through out the zoom range of system, i.e. the separation must be equal to the sum of the focal lengths.

$$D = F_{23} + F_1 = d_1 + \delta. \quad (2.6)$$

Where

$$\delta = d_2 \frac{F_{23}}{F_1} \quad (2.7)$$

by rearranging the above equations, the distance d_1 and d_2 can be expressed as

$$d_1 = F_1 + F_2 + \frac{F_1 F_2}{M F_3} \quad (2.8)$$

$$d_2 = F_2 + F_3 + \frac{M F_2 F_3}{F_1} \quad (2.9)$$

The above equations can be written as

$$d_1 = a_1 + \frac{b_1}{M} \quad (2.10)$$

$$d_2 = a_2 + M b_2 \quad (2.11)$$

where

$$a_1 = F_1 + F_2$$

$$a_2 = F_2 + F_3$$

$$b_1 = F_1 F_2 / F_3$$

$$\text{and } b_2 = F_2 + F_3 / F_1$$

Now by moving a_1 and a_2 to the left hand side and multiplying both the equations will results in

$$(d_1 - a_1)(d_2 - a_2) = b_1 b_2 = F_2^2 \quad (2.12)$$

Which is nothing but the rectangular hyperbola. That rectangular hyperbola will represent the variation of magnitude M w.r.t. d_1 and d_2 . The hyperbola curve will cut the axes at

$$M_x = -\frac{a_2}{b_2} \quad \text{at } d_2 = 0 \quad (2.13)$$

$$M_y = -\frac{b_1}{a_1} \quad \text{at } d_1 = 0 \quad (2.14)$$

The optimal choice of lens focal lengths(F_1 , F_2 and F_3) must be chosen in such a way to achieve the following requirements,

1. d_1 and d_2 are always positive through out the magnification range.
2. System should have positive magnification ($b_2 > 0$).
3. Total system length is less than or equal to 80 mm.
4. Magnification range ($M_x - M_y$) is maximized.

After choosing the optimal lenses, we can replace the paraxial lenses with the

triplets and do the optimization for the final real lens model using the optical simulation software Zemax.

2.4 Results

By using Particle Swarm Optimization, the optimal choice of the lenses is found to be

$F_1 : 80$

$F_2 :-20$

$F_3 :80$

Maximum magnification 3.00

Minimum magnification 0.34

Magnification - 9X

The moments of the lenses (d_1 and d_2), the respective magnification value of the system and the total system length is shown in the figure 2.8. The same system is simulated in Zemax using paraxial lenses, the moment of the lenses and respective magnified images are shown for 3 different configurations in the figures 2.6(a-c) and 2.7(a-c).

Now all the lenses are replaced by real triplets and the complete system is optimized for 52 different configurations (means different combinations of d_1 and d_2) using multi configuration window in Zemax. The resultant system Lens data editor window is shown in the figure 2.12. Moment of the lenses(fig. 2.9) and respective magnified images(fig. 2.10) are shown for 3 different configurations. The values of the separations and magnification are shown in the following figure 2.11 for 14 configurations.

Now the complete bio microscope is designed by placing the eyepiece lens at the end of the system. For eyepiece 80 mm lens is used. Now the complete system is optimized using multi configuration window. Along side the resultant lens arrangements and magnified images for 3 configurations , distortion plots, Seidel aberration plots and spot diagrams are shown in the figure.

It is observed from the results that the distortion values of the complete bio microscope are less than 1% in all the configurations, spot size is also with in the diffraction limit and Seidel aberration values are very less for the complete system. Which are the most desired parametric values that one will target while designing a optical system.

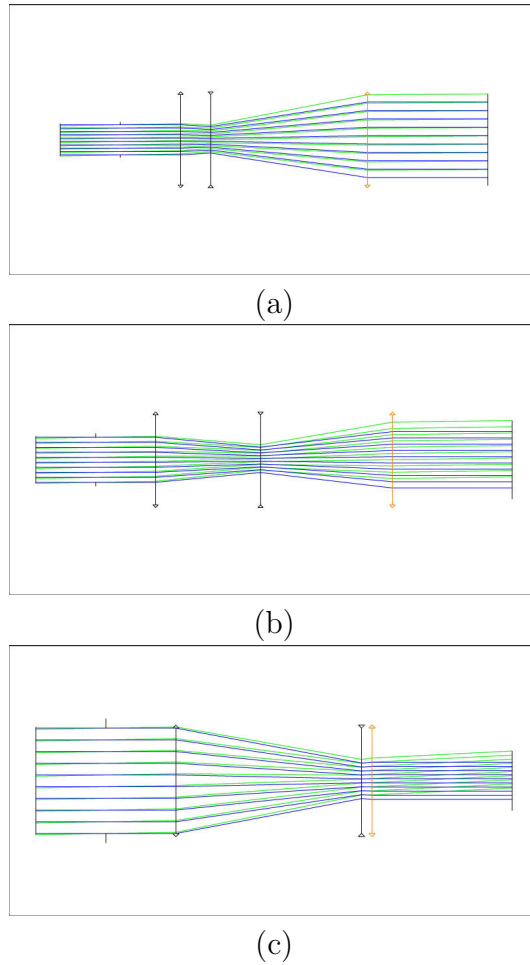
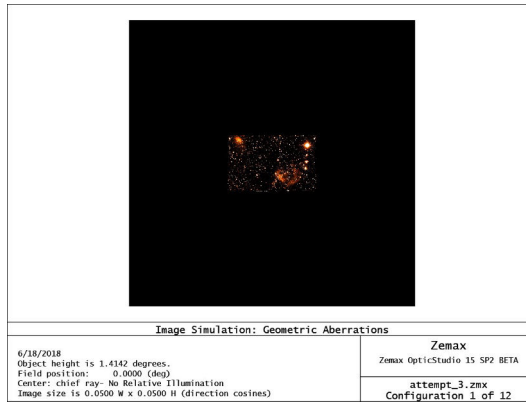


Figure 2.6: Moment of the lenses in afocal system.

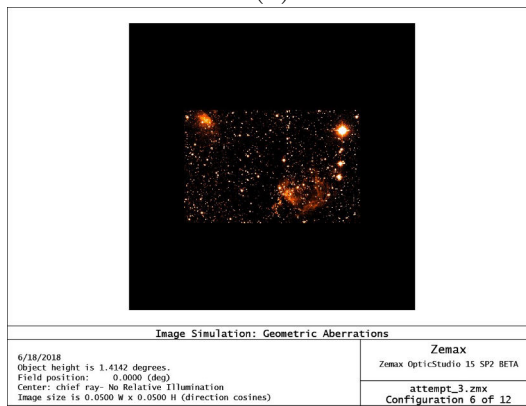
2.5 Discussion and future work

The current problem is focused on the designing of continuous zoom slit lamp camera to replace the well established discrete zoom systems. The parameters of the discrete zoom system are extracted and by keeping these parameters as the final targets zoom system is designed. The key idea behind the design of the continuous zoom is varying the focal length of the second lens of Galilean system by making this lens as the combination of two lenses with variable separation. 3 lens afocal system is formulated and the optimal values of the focal lengths found by using Particle Swarm Optimization. It is found that this system is having more magnification range (9X) than the existing discrete system (6.25X). By using the optical simulation software, the afocal system is design in paraxial domain. Then each lens is replaced by using triplets and optimized using multi configuration window.

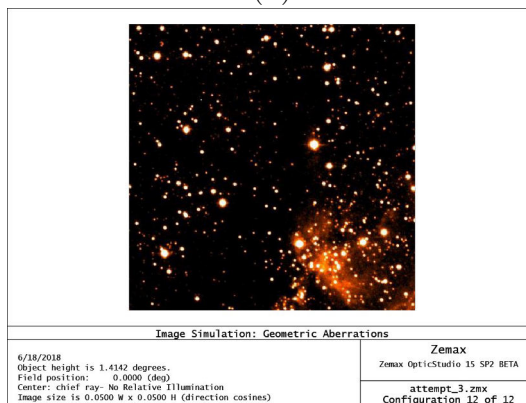
Complete bio microscope is designed by adding a eyepiece to the existing afocal



(a)



(b)



(c)

Figure 2.7: Variation of the magnification of Images with zoom.

system. It is observed from the results that the distortion values of the complete bio microscope are less than 1% in all the configurations, spot size is also within the diffraction limit and Seidel aberration values are very less. Which are the most desired parametric values that one will target while designing an optical system. Though the current study results are good, there are few more optical parameters

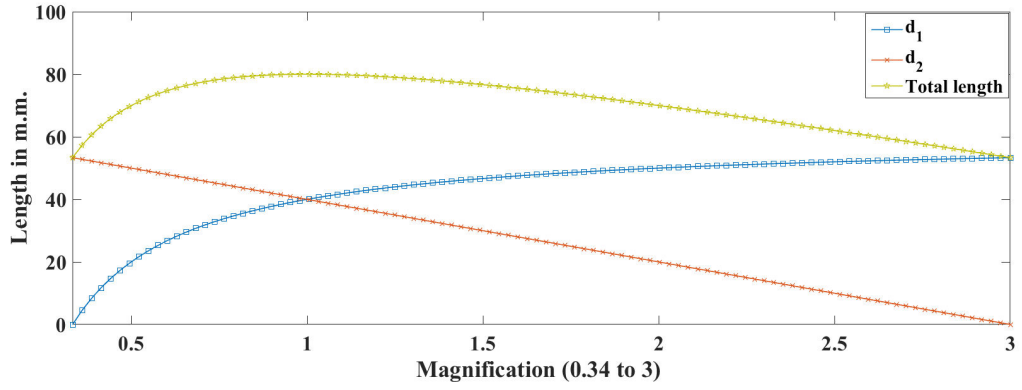


Figure 2.8: The variation d_1 , d_2 and total system length as a function of magnification.

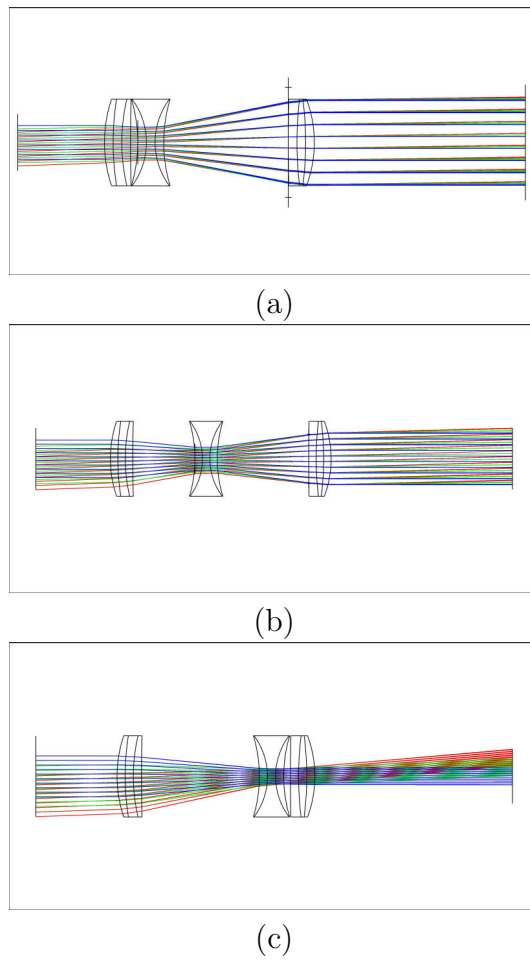
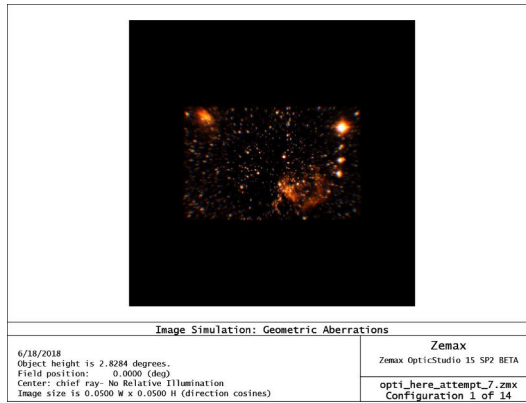


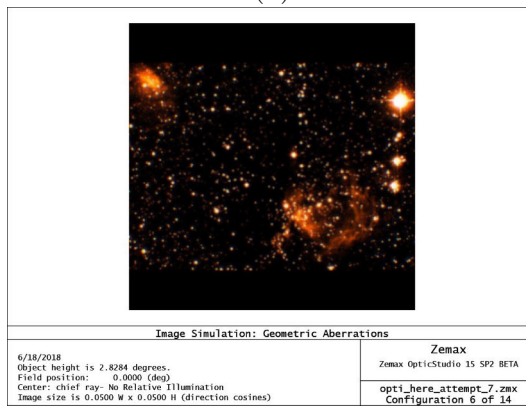
Figure 2.9: Moment of the lenses in afocal real lens system.

like Modulation Transfer Function, Chromatic Focal shift and Point Spread Function need to be considered in the optimization criteria.

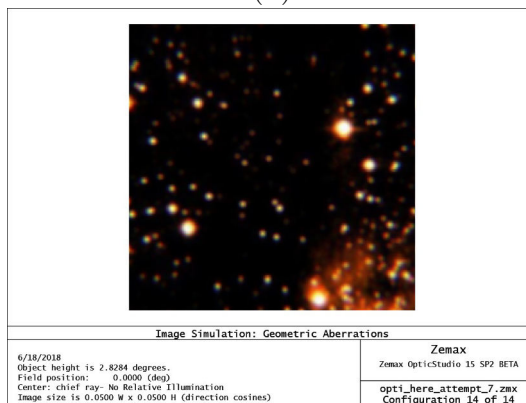
In future, the optimization of choice of the real lens parameters (radius of cur-



(a)



(b)



(c)

Figure 2.10: Variation of the magnification of Images with zoom.

vature, thickness, material and number of lenses) by considering more optical parameters will make the design realistic. Quality assessment, comparison with other zoom systems and real time design will follow the optimization. Finally, the addition of auto focus lens (readily available) as objective lens to the completely optimized system will remove remove the chin rest position of the patients.

Configuration	d_1	d_2	Magnification
1	2.5	43.03	0.4067
2	5	42.67	0.4279
3	10	41.78	0.4780
4	15	40.60	0.5417
5	20	39.00	0.6254
6	25	36.76	0.7403
7	30	33.42	0.9078
8	35	27.97	1.1752
9	39.13	20	1.5577
10	40	17.68	1.6734
11	40.79	15	1.7992
12	42.07	10	2.0406
13	43.09	5	2.2853
14	43.51	2.5	2.4067

Figure 2.11: The variation d_1 , d_2 and total system length as a function of magnitude.

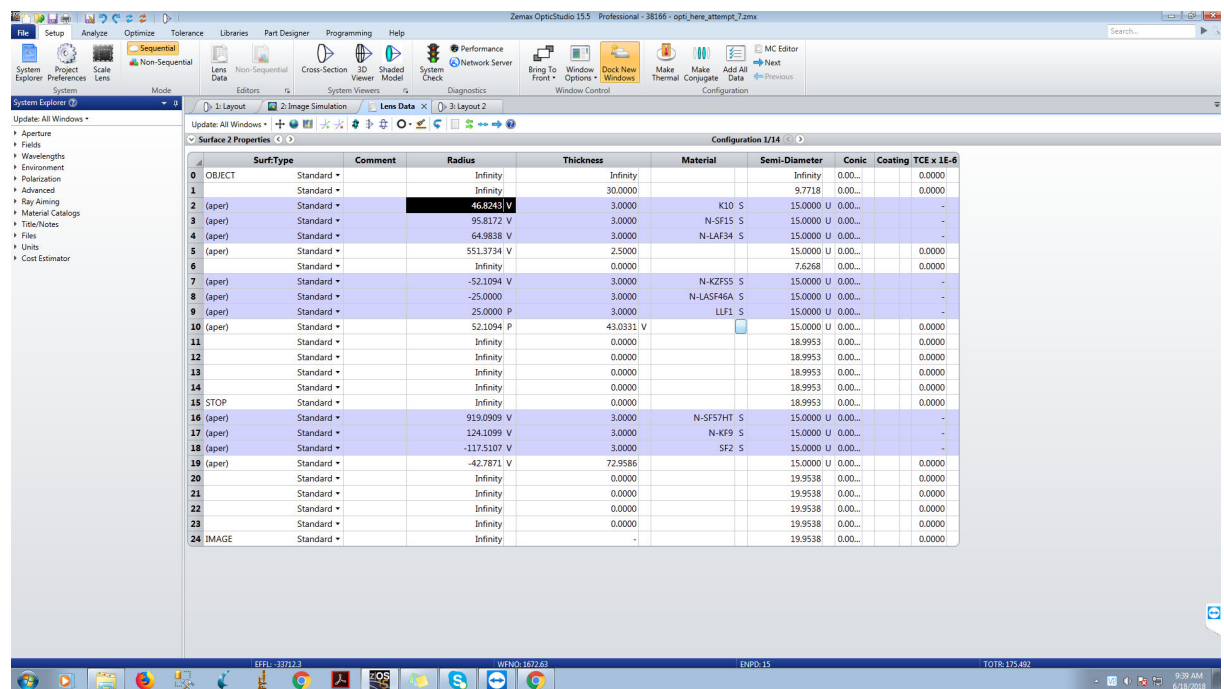
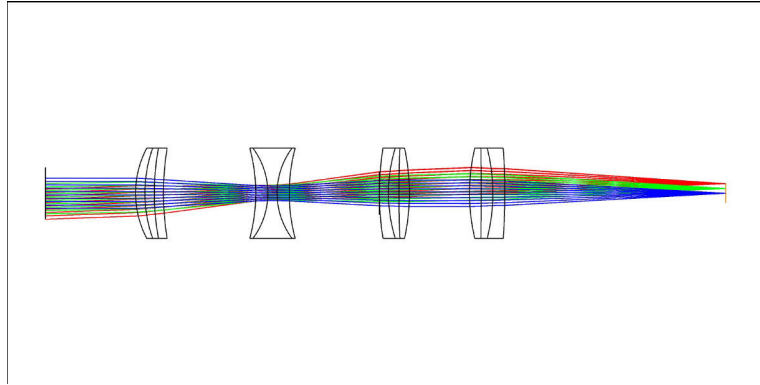
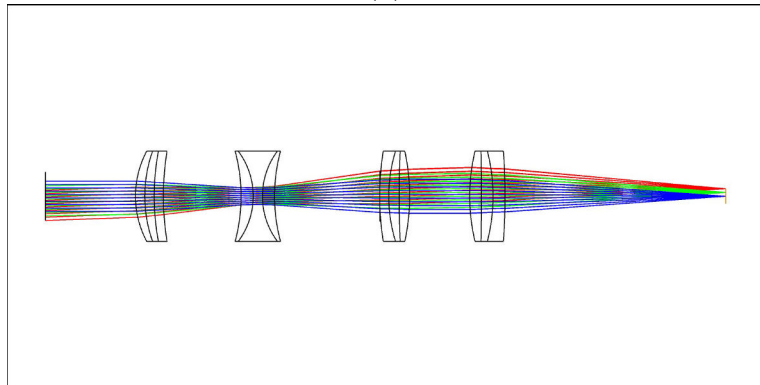


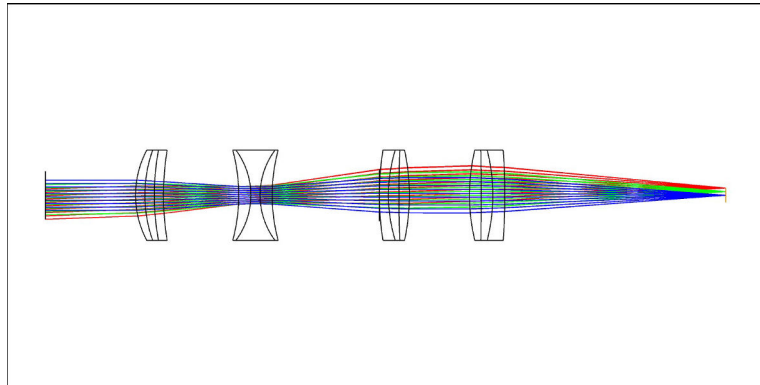
Figure 2.12: The variation d_1 , d_2 and total system length as a function of magnitude.



(a)

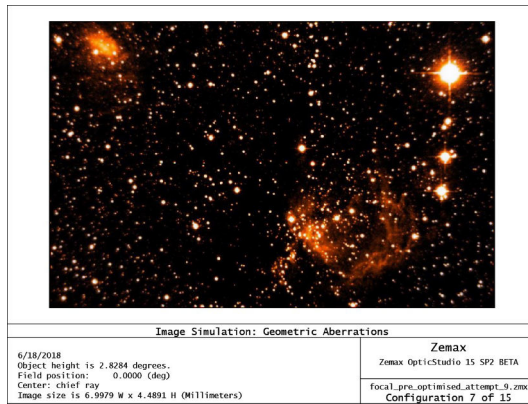


(b)

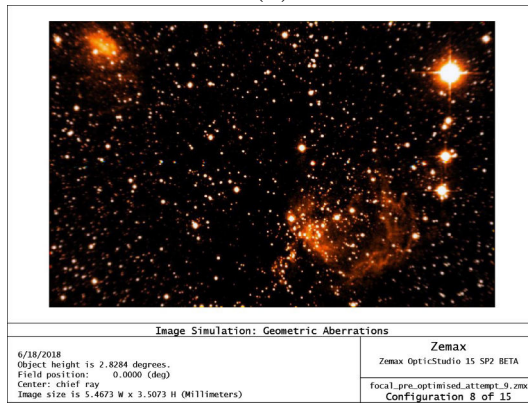


(c)

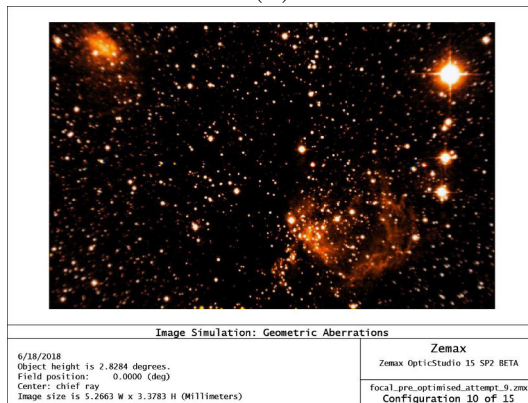
Figure 2.13: Moment of the lenses with zoom.



(a)

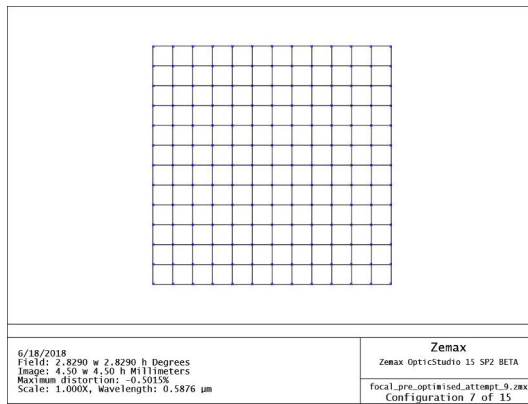


(b)

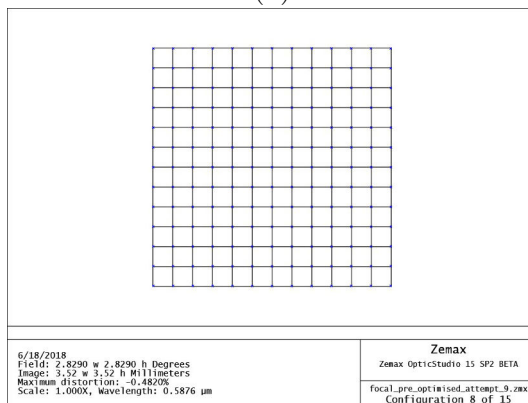


(c)

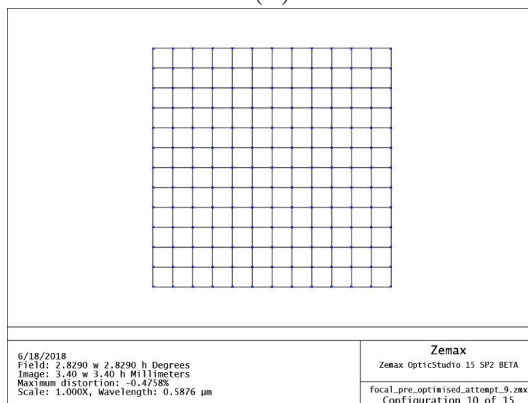
Figure 2.14: Variation of the magnification of Images with zoom.



(a)

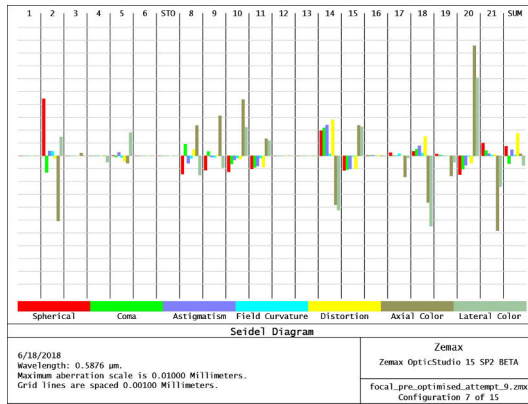


(b)

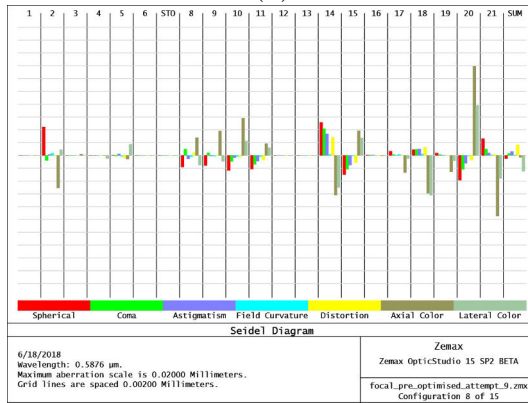


(c)

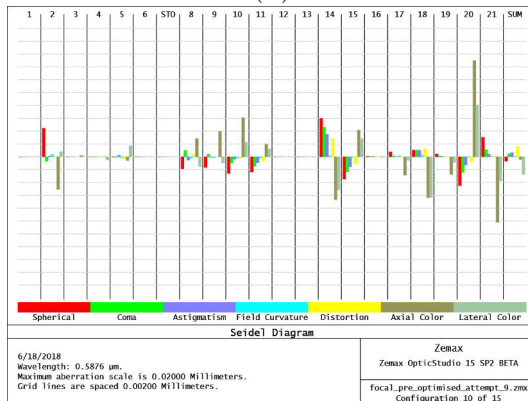
Figure 2.15: Variation of the grid distortion of Images with zoom.



(a)

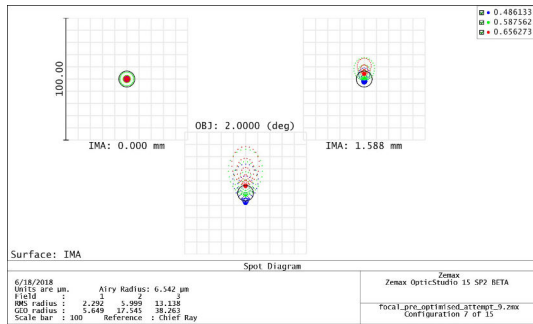


(b)

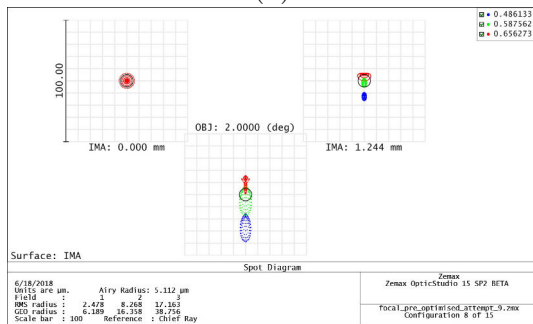


(c)

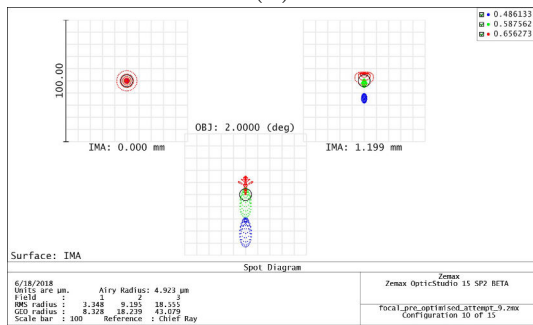
Figure 2.16: Variation of the seidel diagrams of Images with zoom.



(a)



(b)



(c)

Figure 2.17: Variation of the spot diagram of Images with zoom.

Chapter 3

Corneal OCT Analytics

In current ophthalmological practices, assessment of graft condition post Descemet's stripping automated endothelial keratoplasty (DSAEK) is performed qualitatively using few (four) anterior-segment optical coherence tomography (AS-OCT) radial B-scans. From those scans, clinicians need to mentally synthesize the graft in 3D, and estimate its overall condition. In contrast, quantitative representation of 360° thickness profile would facilitate better visualization of graft condition, and hence medical decision making. Consequently, clinicians seek to quantify potential detachments in 3D from the aforementioned sparse B-scans. Against this backdrop, aiming to assist doctors in making an accurate postoperative assessment, we attempted at 3D visualization and quantification of donor lenticule separation (DLS) using only four AS-OCT radial B-scans. It is collaborative work with Kiran Kumar Vupparaboina, a version of it is present in his thesis.

3.1 Introduction

Endothelial keratoplasty (EK) has largely replaced penetrating keratoplasty (PK) as the surgery of choice for diseases exclusively involving the endothelium of the cornea [12]. This transition has marked a significant leap in corneal transplantation procedures because EK replaces only the damaged tissue/layer, while preserving the healthy corneal tissue in the recipient cornea. Further, EK tends to achieve superior spectacle corrected visual outcomes, fast recovery, fewer instances of graft rejection and higher patient satisfaction. Among various EK procedures, Descemet's stripping automated endothelial keratoplasty (DSAEK), a minimally invasive partial thickness corneal transplantation procedure, which replaces diseased tissue with a thin donor graft (lenticule) of posterior corneal stroma, Descemet's membrane and endothelium, is

widely performed. In particular, DSAEK is performed for treating diseases including Fuchs endothelial dystrophy, pseudophakic/aphakic bullous keratopathy, pseudophakic corneal edema, trauma following glaucoma surgery, failed corneal graft and irido-corneal endothelial syndrome [12–14]. Despite its advantage, DSAEK too sometimes lead to complications. The most common one in the early postoperative period is graft dislocation or detachment, with reported dislocation rates varying from 0% to 82% and with an average of 14.5% [15]. Usually graft dislocation is detected within the first day or two, however occasionally the detection may occasionally take several weeks [16]. Initial graft attachment can be impaired by a full-thickness graft edge from a decentered trephination, or by surgical trauma that temporarily or permanently reduces endothelial cell function, or in adequate intraoperative air tamponade or leaky wounds/postoperative hypotony or rubbing or squeezing the eye in the early postoperative period [16, 17]. Detached grafts can reattach spontaneously, or be reattached by repositioning the graft and injecting an air bubble intra-camerally, in a process called re-bubbling [18].

In making clinical judgement, the detachment profile plays an important role. The detachment can be communicative (i.e., in contact with aqueous humor) or non-communicative (i.e., not in contact with aqueous humor). Such categorization assumes clinical significance because non-communicative separations have a higher probability of reattachment over time. Ideally, an expert should also know the thickness profile and the volume of the detachment in order to accurately decide whether further surgical intervention is necessary. There has been no literature on quantification of amount of detachment and a treatment algorithm that can be used to decide on second intervention like re-bubbling. There have been reports of spontaneous attachment of detached grafts but the literature does not provide evidence on when to observe. This study is an attempt to identify a quantification method that could be validated and aid in decision making.

AS-OCT has played an important role in identifying corneal pathologies and also in planning for surgery [19]. It helps in localizing the corneal pathology in different layers. It also helps in assessing the attachment of graft postoperatively after DMEK or DSAEK. Further, the recent introduction of the intraoperative OCT (*i*OCT) really helps in performing lamellar keratoplasties more precisely with real time visualization of the corneal layers [20]. Recently, *i*OCT was also used to understand the association between transient interface fluid (TIF) and textural interface opacity (TIO) following DSAEK [21]. Frequency domain OCT (FD-OCT) systems provide scans in two modes (i) single high resolution B-scan covering entire corneal cross section; and (ii) raster

scans covering a portion of cornea. On the other hand, time domain OCT (TD-OCT) systems capture a maximum of four radial scans covering full cornea (10mm scan width) taken at an angular separation of 45° . In view of this, the ophthalmologist makes a subjective estimation of the type and extent of separation by examining the TD-OCT radial scans. See Figs. 3.1a–d for radial AS-OCT scans of a subject post DSAEK, with recipient cornea, donor lenticule and the detachment between those labeled. Also see Fig. 3.1e for depiction of angular locations of those scans. Based on those four 2D sections, the physician in effect synthesizes the 3D topological variation of the detachment mentally. This may lead to unacceptably large subjective variations in medical decisions. The problem could amplify when it comes to monitoring the evolution of such separation with time, especially, if multiple physicians are involved. As a remedy, clinicians seek to objectively quantify the graft detachment after DSAEK. Further, quantitative examination could be crucial in the recently introduced intraoperative OCT [20, 21]. To this end, it is imperative to develop an automated tool that enables clinicians to visualize and quantify topographical variation of the detachment. In particular, such a tool should accurately detect the type of separation (either communicative or non-communicative), and estimate thickness profile and the volume of the detachment.

Automated quantification of corneal thickness has recently been attempted, aiming at monitoring corneal edema and endothelial function, managing ocular hypertension and planning common keratorefractive surgeries such as laser-assisted in situ keratomileusis (LASIK) and photorefractive keratectomy (PRK) [22–27]. However, to the best of our knowledge, automated analysis post DSAEK has hitherto not been attempted. Note that automated quantification of corneal thickness in traditional corneal transplant where the complete cornea is replaced poses relatively less challenge. In comparison, DSAEK tends to pose significant challenge because (i) the detachment could be either complete or partial (at central or peripheral corneal locations); (ii) the relatively dark intensity profile of the detachment could be confounded by that of aqueous humor as well as the outside region; and (iii) of the limited number (four) of scans available to estimate the complete thickness profile (over 360°) of detachment and other corneal regions. In response, we proposed a novel methodology to detect the detachment and estimate its profile. In particular, we viewed the detachment as a tube-like structure in 2D, and detected it using Hessian matrix analysis [28]. Subsequently, a two-stage interpolation was employed to obtain the 3D profile of the detachment. The proposed methodology was tested on 27 eyes (belonging to unique patients), amounting to 108 radial OCT images altogether. Performance

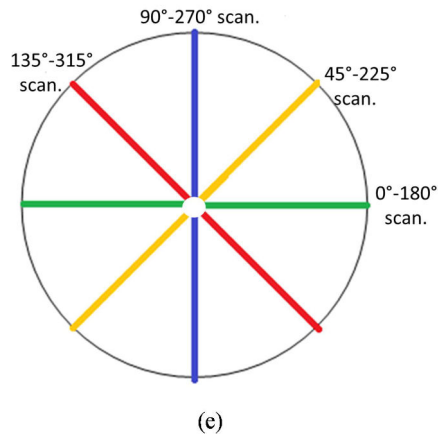
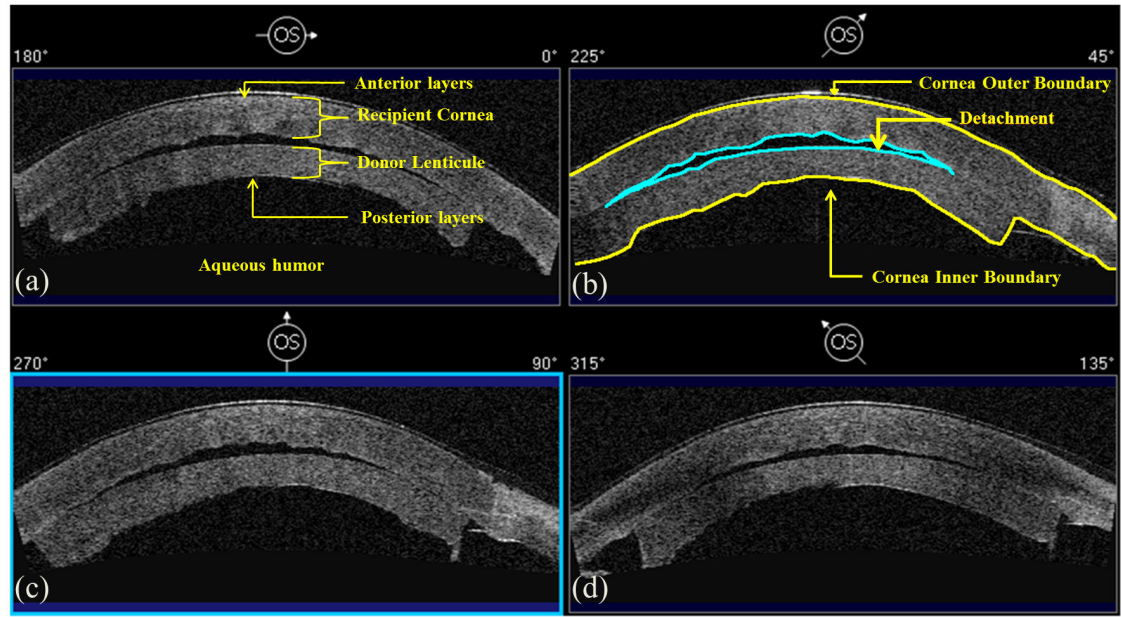


Figure 3.1: (a)–(d). Typical AS-OCT radial scans of a subject taken with 45° separation post DSAEK. (e) Graphical representation of locations of four radial scans captured.

of algorithmic segmentation of detachment was evaluated vis-à-vis that of manual delineations, taking both intra- and inter-observer repeatability into account.

The rest of the chapter is organized as follows. Section 2 details the data acquisition and the proposed methodology. Subsequently, Section 3 presents experimental results and statistical performance analysis. Finally, Section 4 concludes the work with discussion.

3.2 Methods

3.2.1 Data acquisition

The present study was performed, from July 2008 to June 2015, at Tej Kohli Cornea Institute, L. V. Prasad Eye Institute, Hyderabad, India. Approval from the Institutional Review Board of the institute was obtained and the subjects provided their informed consent. Further, this study was conducted in accordance with the tenets of the Declaration of Helsinki. During the study period, 2260 eyes underwent DSAEK and 96 (4.2%) eyes developed graft detachment that was managed by re-bubbling.

Inclusion criteria: All patients who had DSAEK/DSEK and had a graft detachment on the first postoperative day. The patients who had graft detachment and had an AS-OCT done on the first postoperative day.

Exclusion criteria: The patients who have not undergone OCT examination inspite of the graft detachment.

In particular, 27 eyes from unique patients, who had graft detachment on the first postoperative day after DSAEK, were included in the study. On each eye, 4 AS-OCT scans were obtained using Visante AS-OCT (Carl Zeiss Meditec, Dublin, CA). Scans were acquired with a maximal scan velocity of 2000 axial scans per second. Further, each scan spans 6mm (depth) \times 16mm (width) area with a axial resolution of 18 μ m and lateral resolution of 60 μ m. All scans were performed by a trained optometrist.

Manual segmentation: Accuracy of the proposed algorithm for segmenting the detachment was compared against the manual segmentations. Two trained observers carried out manual delineation of detachment regions. In particular, manual segmentations were performed using freehand selection tool of ImageJ software version 1.47 (courtesy Wayne Rasband, National Institutes of Health, USA) [29]. In each image, detachment boundaries were marked twice by each observer, masked to previous attempts. These segmentations were taken as baseline to compare to evaluate the accuracy of the proposed method. In order to perform unbiased evaluation, we considered average of all four delineations as the reference, against which the outcome of the proposed method was compared.

3.2.2 Proposed Methodology

The proposed methodology is schematically depicted as a flowchart in Fig. 3.2. Major steps include (i) localization of cornea, (ii) demarcation of detachment, and (iii) 3D mapping. Each of these substeps is elaborated in the following.

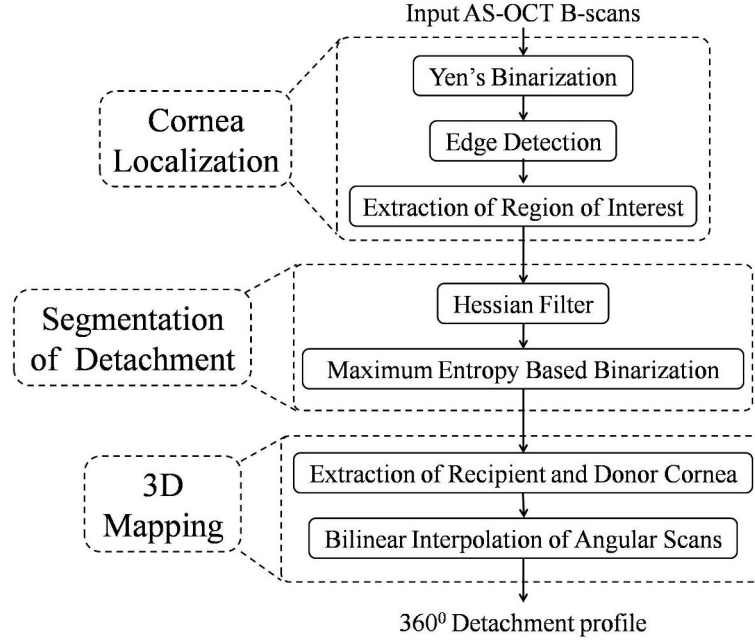


Figure 3.2: Schematic of proposed methodology.

Cornea Localization

A typical AS-OCT image taken post DSAEK consists of recipient cornea and donor graft, either attached or detached (see Fig. 3.1), and background (granular). The background contains speckle noise, prominently visible in parts of the image depicting aqueous humor (clear fluid between cornea and lens) and air outside eye ball. In case of detachment, the space between recipient and donor cornea is also filled with fluid (aqueous humor in the communicative case). As a result, the detachment and the background regions appear to acquire similar intensity profile, making the desired segmentation of the detachment region difficult. The segmentation becomes particularly difficult in the communicative or partially communicative cases. In this backdrop, we localized the cornea between corneal outer and inner boundaries (see Fig. 3.1a) to facilitate the desired segmentation.

Specifically, we first binarized the OCT B-scan by employing Yen’s thresholding [30,31], which was empirically found to mitigate artifacts arising due to intensity inhomogeneity (Fig. 3.3a). Subsequently, corneal outer boundary is detected by finding the first significant intensity gradient while scanning each column of the binarized image from top to bottom (Fig. 3.3b). However, in certain instances, presence of tear film and other prominent reflections could confound the detection of corneal outer boundary (see Fig. 3.4a). In particular, tear film affects the estimate of corneal

thickness and may possibly get detected as a false detachment (see Fig. 3.4b). To surmount such effect, morphological open-close operation using a disk structuring element (radius = 2 pixels) was performed in the neighborhood (10 pixels above and 50 pixels below) of the previously detected upper edge. Subsequently, proceeding in the same vein as earlier, we obtain the initial estimate of the corneal outer boundary by scanning each column of the image (Fig. 3.4c). Finally, we perform circle-fitting [32] on the initial estimate to smoothen the spurious points arising at the central cornea potentially due to high reflections from the tear film (Fig. 3.4d).

Next, we proceed to detecting corneal inner boundary from the binarized image. While the outer boundary is completely defined by recipient cornea, the inner boundary is defined as the envelope of posterior parts of both recipient and donor corneal regions. Accordingly, to find corneal inner boundary, we first obtain the largest connected component from the binarized image [33]. Further, we also obtained the second largest connected component if it was at least greater than ten percent of the size of the largest connected component (corresponds to donor graft in case of communicative detachment). Subsequently, we scanned for first significant intensity gradient from the bottom to top of each column in the image to obtain initial estimate of corneal inner boundary (Fig. 3.3d). However, this estimate sometimes contains spurious spikes/dips, especially, at the central location, due to high reflectivity of the pixels (Fig. 3.5a–b). In such cases, we detected the location and extent of the dip and then perform linear interpolation to obtain desired corneal inner boundary (Fig. 3.5c). Finally, region between the detected corneal inner and outer boundaries is marked as the region of interest (ROI).

Segmentation of Detachment

We now proceed to algorithmically detect the detachment within the ROI obtained in the previous step. However, detecting the detachment is not straightforward, specifically, due to inhomogeneity of intensity levels in the detachment region and in the corneal regions. Here, methods such as intensity based thresholding could be inaccurate. In view of this, we primarily perform Hessian matrix analysis which has elsewhere been used to find dark tubular structures like blood vessels in medical images [28]. Interestingly, in 2D sections, the detachment region appears approximately as a planar projection of dark tubular structure, where eigenvalues of the detachment region differ from that of the corneal region. This method is adopted to demarcate the detachment. Specifically, at every pixel inside the ROI, we compute the eigenvalues

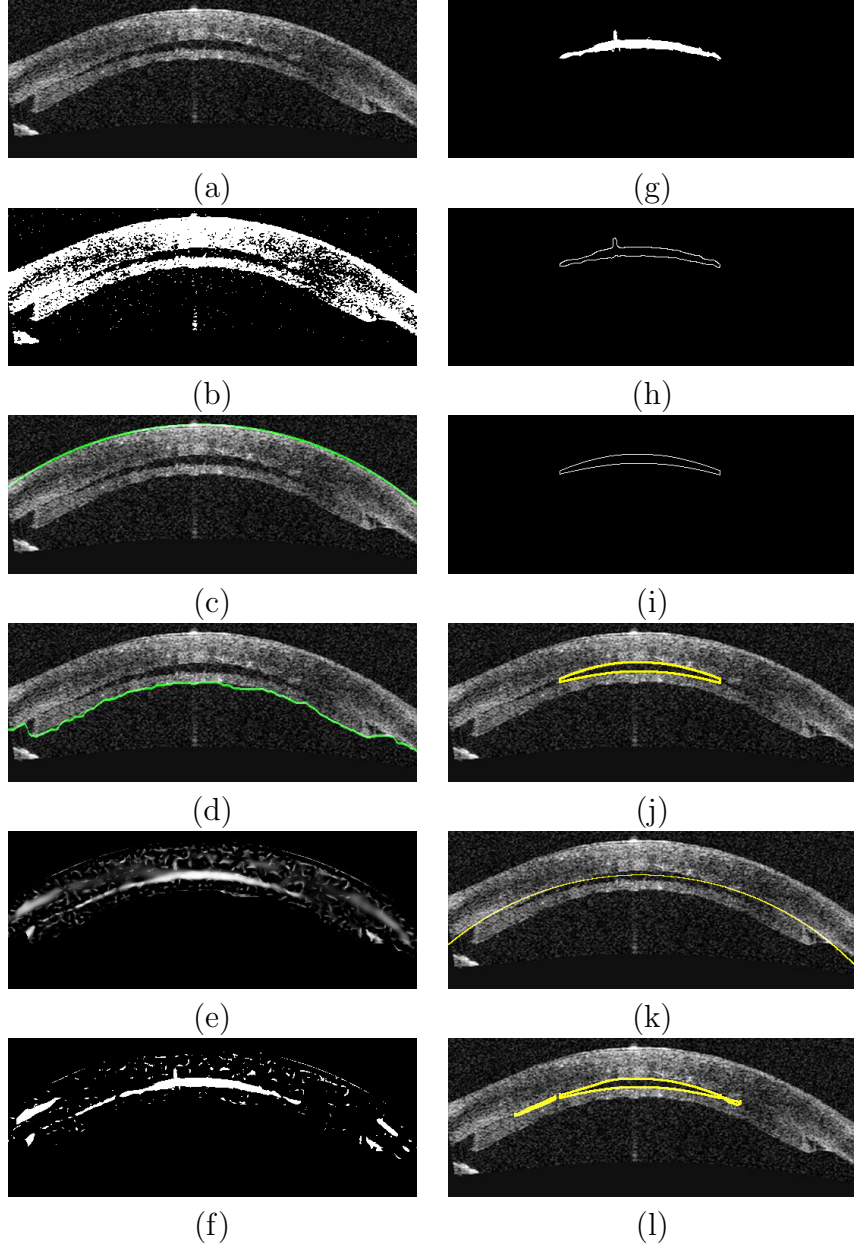


Figure 3.3: Graphical representation of proposed methodology: (a) AS-OCT image, (b) Yen's thresholding, (c) Detected cornea outer boundary, (d) Detected cornea inner boundary (e) Vesselness-filtered estimate in ROI, (f) Maximum entropy criteria thresholding on vesselness-filtered estimate, (g) Initial estimate of the detachment by extracting biggest connected component (h) Contour of the initial estimate, (i) Smoothened initial estimate, (j) Initial estimate overlaid on the image, (k) Central line passing through the detachment, and (l) Final estimate of the detachment after detecting connected components along the central line.

λ_1 and λ_2 ($|\lambda_2| > |\lambda_1|$)¹ of the estimated Hessian matrix H of a 2×2 neighborhood.

¹The fact that different relationships between the eigenvalues define various tube-like structures has been utilized in detecting blood vessels [34].

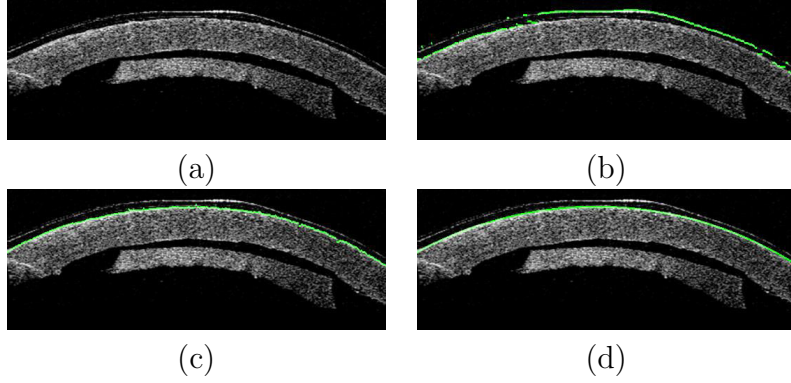


Figure 3.4: Detailed illustration of cornea outer boundary detection: (a) AS-OCT image, (b) Initial estimate obtained by reading first significant intensity gradient (c) Estimate after performing morphological open-close operation and (d) Final estimate after circle fitting.

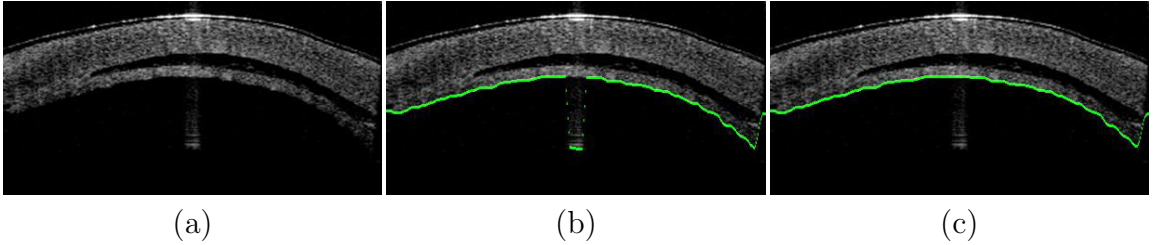


Figure 3.5: Detailed illustration of cornea outer boundary detection: (a) OCT image, (b) Initial estimate obtained by reading first significant intensity gradient from bottom and (c) Final estimate after removing the spurious dip at the center.

Then we apply the so-called ‘vesselness filter’ developed to detect vessels [34]

$$V(x, y) = \begin{cases} 0 & \text{if } \lambda_1 > 0 \\ \exp(-\frac{R_\beta^2}{2\beta^2})(1 - \exp(-\frac{S}{2c^2})) & \text{otherwise} \end{cases} \quad (3.1)$$

at every pixel location (x, y) . Here $R_\beta = \lambda_1/\lambda_2$ denotes the ‘blobness’ measure in 2D, indicating the deviation from a blob-like structure, $S = |H| = (\lambda_1^2 + \lambda_2^2)^{1/2}$ denotes the second order ‘structuredness’, and β and c (empirically set to $\beta = 0.5$ and $c = 15$) denote thresholds controlling the sensitivity of the filter to the measures. Note that for an ideal tubular structure, we have $V(x, y) = 1$, while for a non-tubular structure, we have $V(x, y) = 0$. In practice, $V(x, y)$ should be high for tube-like structures. In this connection, Fig. 3.3e depicts the vesselness-filtered output where the $V(x, y)$ values within the detachment appears to be high. Subsequently, to extract the detachment, we perform maximum entropy criteria (MEC) thresholding [35] on vesselness-filtered output to segregate the background and the foreground

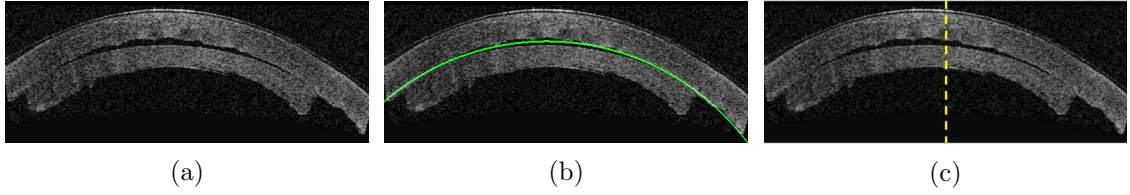


Figure 3.6: (a) OCT image; (b) Extraction of recipient cornea and donor lenticule based on central axis (green line) of detachment; and (c) dividing OCT image into two halves based central axis (yellow dotted line) to facilitate 3D mapping.

(detachment) regions (Fig. 3.3g). Here the detachment corresponds to the largest connected component which is extracted and smoothed in Fig. 3.3g–j). However, in some cases, there could be multiple detachments and hence extracting only the largest connected component may not be sufficient. In view of this, we employ postprocessing to identify significant blobs lying close to the central axis (Fig. 3.3k) of the largest connected component within the extent of the donor lenticule (Fig. 3.3l).

3D Mapping

As alluded earlier, clinicians make qualitative assessment based on four radial scans taken at 45° difference. However, such assessment hardly takes into account the complete picture of the 3D topology of the detachment, and the 3D thickness profile of the cornea (including recipient and donor lenticules). In this context, we now proceed to map the detachment and corneal regions in 3D. To this end, we begin by delineating in 2D the recipient and the donor corneal tissues in addition to the aforementioned detachment region in each of the four radial scans. A typical AS-OCT scan is reproduced in Fig. 3.6a. To this, the central line is added in Fig. 3.6b. To compute the central line, the corneal outer boundary is first approximated by a circular arc. Next, keeping its center fixed, the radius is reduced so that the modified arc provides the best fit (in the least squares sense) the midpoints of the detached region along all columns, and such arc is referred as the center line. At this point, based on the fact that only pixels with nonzero intensities belong to tissues, the recipient and donor corneas are distinguished as follows. The nonzero pixels outside the central line are taken to constitute the recipient cornea, whereas those inside the central line are taken to constitute the donor cornea.

Next, we perform angular interpolation of the delineated 2D regions to obtain the 3D profile. To this end, we first identify in each of the four radial scans the corneal peak, which divides each delineated region into two halves (Fig. 3.6c). For each eye, altogether we thus obtain 8 such halves, using which the angular interpolation is

performed. In particular, equiangular sections are considered between two adjacent halves, and the outer and the inner edges of respective regions are linearly interpolated from those halves. In the course, those edges are approximated as piecewise linear to simplify the process. To be specific, we consider 100 linear pieces for each of outer and inner edges per half scan. The method of interpolating the aforementioned edges from two observed halves at 45° to a synthetic half-section at an intermediate angle is illustrated from different views in Figs. 3.7a–c. Finally, we interpolate such edges to half-sections chosen at 1° angular resolution. This operation is depicted at low angular resolution in Figs. 3.7d–f (from three different perspectives), and slightly higher angular resolution in Figs. 3.7g–i (from three different perspectives again). Note that we still have only half-sections, albeit as a fine angular resolution. We obtain desired surfaces differentiating recipient and donor corneas as well as the detachment region in 3D via morphological closing. Figure 3.8 depicts 3D mapping of detachment and corneal regions in various combinations.

3.2.3 Reference Performance: Inter-Observer Repeatability

Towards analyzing the algorithmic segmentation, we first attend to certain engineering considerations involving performance.

Dice coefficient

In view of quantitative analysis, it is important to consider appropriate evaluation criteria that compares algorithmic and manual segmentations of the detachment region. Accordingly, as a natural pick, one might be tempted to use difference in areas of the detachments regions obtained by two methods. While such criteria was found appropriate for many cases, it may not rightly capture the closeness of the two segmentations at hand, especially when the segmented detachment regions obtained by two methods are non overlapping but has equal areas [36]. In this context, we seek a metric that captures the extent overlap of regions obtained by two delineations. To this end, we employ Dice coefficient (DC) which captures the desired property between detachment region obtained by different methods and is given by [37]

$$\text{DC} = \frac{2\text{Area}(d_1 \cap d_2)}{\text{Area}(d_1) + \text{Area}(d_2)}. \quad (3.2)$$

for two competing delineated regions d_1 and d_2 .

In particular, we obtained four manual delineations for each image performed twice

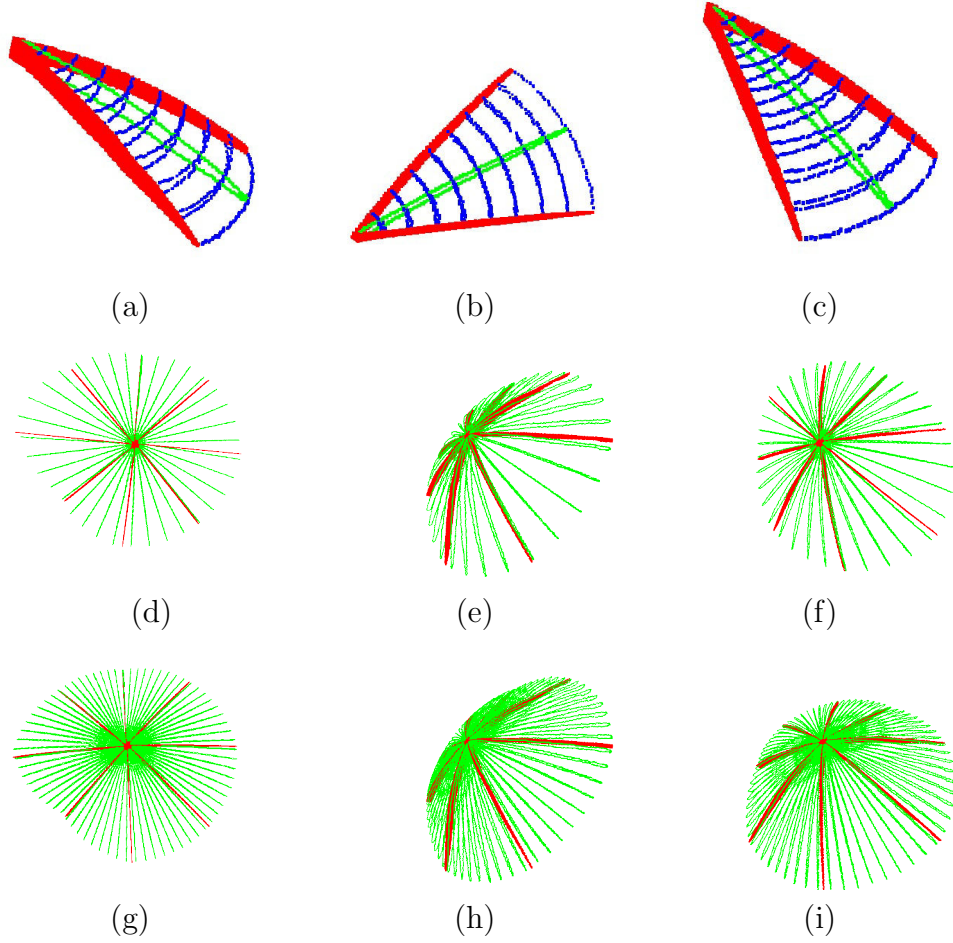


Figure 3.7: Interpolation to obtain intermediated scans: (a)–(c) Intermediate 100 points (green dotted line) on the lines (blue dotted lines) obtained by interpolation of 100 equidistant points chosen on upper and lower boundaries of detachment region extracted from 0° and 45° scans (red regions); (d)–(f) Different views of four interpolated regions (green contour) obtained between adjacent 45° segments (red) extracted; (g)–(i) Different views of eight interpolated regions (green contour) obtained between adjacent 45° segments (red) extracted.

by two observers such that both the observers are masked to their earlier markings and to each others. In this setting, we measure the observer repeatability in terms of Dice coefficient which is used as a yardstick for evaluating algorithmic performance. In particular, we measure both intra- and inter-observer repeatability as follows. For the j -th observer ($j \in \{A, B\}$), the intra-observer DC is given by

$$\text{DC}^{\text{intra}^j} = \frac{2\text{Area}(\text{M1}^j \cap \text{M2}^j)}{\text{Area}(\text{M1}^j) + \text{Area}(\text{M2}^j)}, \quad (3.3)$$

where $M1^j$ and $M2^j$ are the two manual segmentations performed by the j -th observer. In the same vein, the inter-observer DC is given by

$$DC^{inter} = \frac{4Area(M1^A \cap M2^A \cap M1^B \cap M2^B)}{Area(M1^A) + Area(M2^A) + Area(M1^B) + Area(M2^B)} \quad (3.4)$$

based on four segmentations $M1^A$, $M2^A$, $M1^B$ and $M2^B$. Recall that our dataset consists of $N = 108$ AS-OCT images taken from 27 eyes. Hence, using formulas (3.3) and (3.4), we compute for the i -th image respective intra- and inter-observer DCs $DC_i^{intra^j}$ ($j \in \{A, B\}$) and DC_i^{inter} , $i = 1, 2, \dots, N$.

Furhter, the mean DC is given by $MDC = \frac{1}{N} \sum_{i=1}^N DC_i$, and the standard deviation in DC by $SDDC = \sqrt{\frac{1}{N} \sum_{i=1}^N (DC_i - MDC)^2}$. In Table 3.1, note that intra-observer repeatability values for both the graders A and B, respectively, $MDC^{intra^A} = 94.06\%$ and $MDC^{intra^B} = 93.63\%$ were found to be approximately equal, and relatively high. Also, the respective standard deviations $SDDC^{intra^A} = 2.99\%$ and $SDDC^{intra^B} = 2.88\%$ are also close, and relatively low. These indicate that each grader was almost equally consistent between attempts. In contrast, the inter-observer repeatability value of $MDC^{inter} = 86.77\%$ is relatively low, whereas the associated standard deviation $SDDC^{inter} = 5.11\%$ is relatively high. These in turn indicate that graders A and B had dissimilar individualized biases. The aforementioned conclusions are also supported by the fact that the minimum-maximum spread is comparable between the graders A and B for the intra-observer case, but is significantly higher for the inter-observer case. Next, as inter-observer repeatability is less prone to individualized biases, we take that as the manual reference for performance, and set $MDC^{ref} = MDC^{inter}$. From now onward, the superscript ‘*ref*’, standing for reference, will be used in place of the superscript ‘*inter*’. As explained above, inter-observer repeatability provides a more robust reference than intra-observer repeatability, but requires recruitment of multiple graders rather than that of single grader.

3.2.4 Algorithmic Performance Criteria

Taking inter-observer repeatability as the reference, we now proceed to define a performance index for our automated algorithm. While the desired index DC^{auto} for an arbitrary image should ideally be measured by the DC between the manual segmentation and the algorithmic segmentation P, we cannot have such a direct measure because we have four manual segmentations $M1^A$, $M2^A$, $M1^B$ and $M2^B$ rather than one. Taking this into account, and proceeding as outlined in our earlier work [36], we

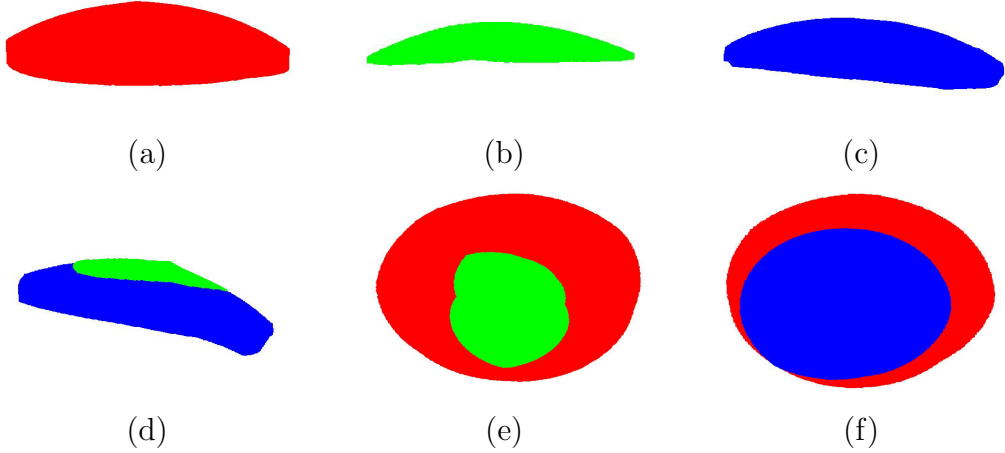


Figure 3.8: 3D visualization: (a) Recipient cornea; (b) Detachment region, (c) Donor lenticule, (d) Detachment and donor lenticule regions together, (e) Detachment and recipient regions together, (f) Recipient and lenticule regions together.

obtain

$$DC^{auto} = \frac{Area(P \cap M1^A) + Area(P \cap M2^A) + Area(P \cap M1^B) + Area(P \cap M2^B)}{2(Area(P) + (Area(M1^A) + Area(M2^A) + Area(M1^B) + Area(M2^B))/4)}. \quad (3.5)$$

In particular, we compute DC_i^{auto} for the i -th image, $i = 1, 2, \dots, N$. Hence, we compute the mean and standard deviation MDC^{auto} and $SDDC^{auto}$, respectively.

3.3 Results

The proposed algorithm was evaluated on 27 eyes from unique patients (both male and female) treated with DSAEK. As mentioned earlier, four radial OCT B-scans with 45° angular separation were obtained for each eye. Using these images, we now evaluate performance of the proposed algorithm qualitatively and quantitatively. In this connection, algorithmic segmentation results alongside manual delineations for four representative eyes are presented in Fig. 3.9 for subjective evaluation. Algorithmic delineations appear desirably close to manual ones. Next we proceed to quantitative evaluation of algorithmic performance. Subsequently, we present desired thickness and volume profiles obtained using our algorithm.

As presented in Table 3.1, we achieved algorithmic mean performance $MDC^{auto} = 81.35\%$ against the reference $MDC^{ref} = 86.77\%$, with respective standard deviation $SDDC^{auto} = 7.55\%$ vis-à-vis $SDDC^{ref} = 5.11\%$. In other words, the automated algorithm performed close to the manual reference. Also, the minimum-maximum

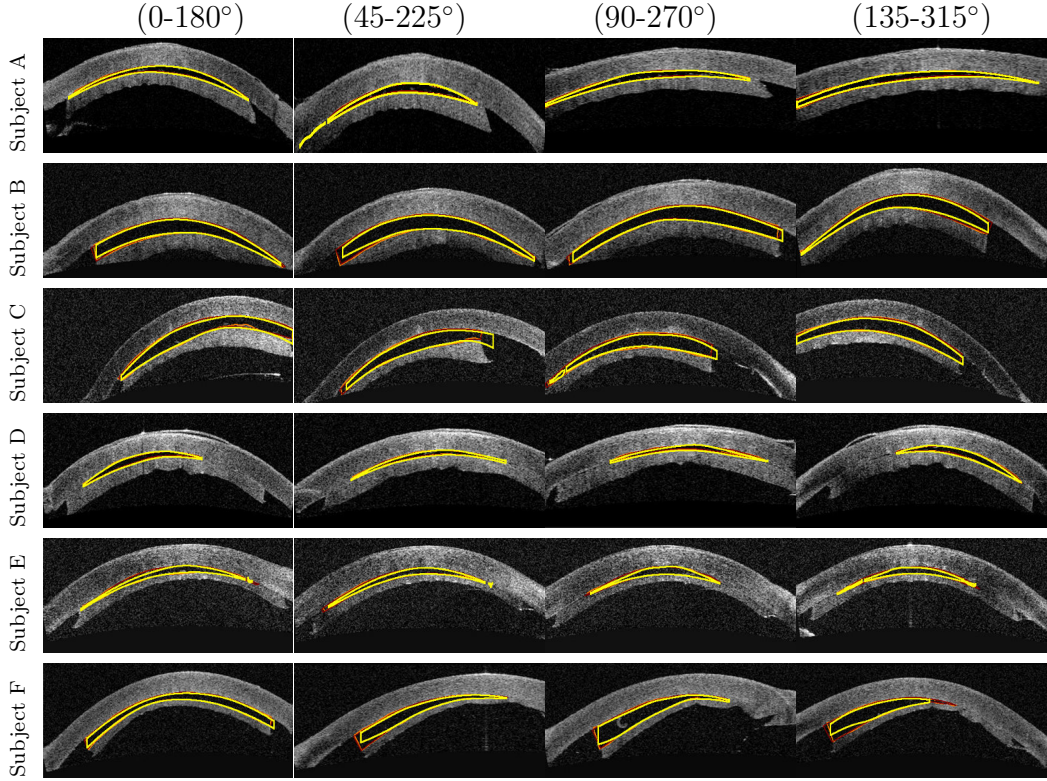


Figure 3.9: Qualitative comparison of segmentation of detachment achieved by proposed method (yellow) and manual methods (maroon and orange) on radial AS-OCT scans of five representative subjects.

Table 3.1: Intra- vs Inter-observer repeatability. Notation: M^A – Manual segmentations by observer A, M^B – Manual segmentations by observer B, M – Manual reference (average).

Evaluation criteria	Method	Parameter	Unit	Value
Dice coefficient (DC)	Manual (intra ^A) ($M1^A$ vs $M2^A$)	MDC (SDDC)	% (%)	94.06 (2.99)
		Min–Max	%	79.53–97.91
	Manual (intra ^B) ($M1^B$ vs $M2^B$)	MDC (SDDC)	% (%)	93.63 (2.88)
		Min–Max	%	84.15–98.16
	Manual (inter) (M^A vs M^B)	MDC (SDDC)	% (%)	86.77 (5.11)
		Min–Max	%	64.45–94.52

spread for our algorithm is slightly larger than that for the manual reference. At this point, we take a detailed look at how the proposed algorithm performed vis-à-vis the reference.

Accordingly, with reference to inter-observer repeatability, we obtained $QMDC = 1.40$ and $QCVDC = 1.57$ (Table 3.2), which are close to one, indicating the efficiency of the proposed algorithm.

Table 3.2: Statistical analysis based on Dice coefficient.

Evaluation criteria	Method	Parameter	Unit	Value
	Automated	MDC^{auto} ($SDDC^{auto}$)	% (%)	81.35 (7.55)
		Min–Max	%	56.85–93.46
		$CVDC^{auto}$	ratio	0.0928
Dice coefficient (DC)	Manual reference	MDC^{ref} ($SDDC^{ref}$)	% (%)	86.77 (5.11)
		Min–Max	%	64.45–94.52
		$CVDC^{ref}$	ratio	0.0589
	Quotients	QMDC	ratio	1.40
		QCVDC	ratio	1.57

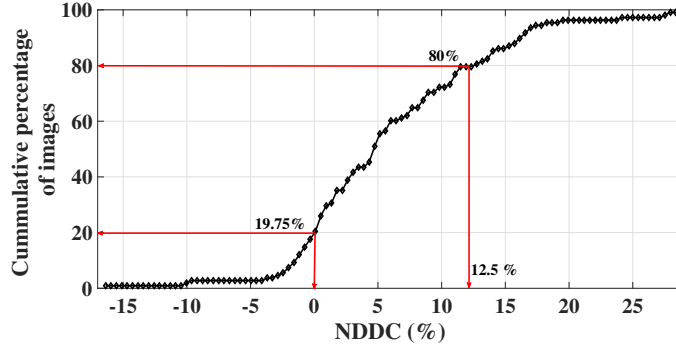


Figure 3.10: Normalized difference in DC between proposed (DC^{auto}) and manual (DC^{inter}) methods.

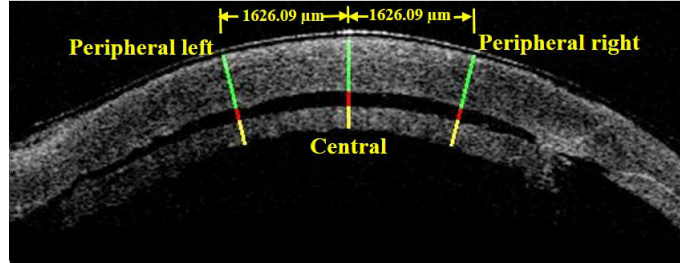


Figure 3.11: Thickness estimates for recipient cornea (green) and donor lenticule (yellow) at central and peripheral locations.

3.3.1 Thickness estimates of recipient cornea and donor lenticule

Central corneal thickness (CCT) is routinely used to monitor corneal edema and endothelial function, manage ocular hypertension and plan common keratorefractive surgeries such as LASIK and photorefractive keratectomy (PRK) [22–27]. In particular, a gradually thickening graft could be failing, and a sudden thickening signals rejection. Further, the intra ocular pressure (IOP) is related to corneal thickness. In

Table 3.3: Thickness estimates of recipient cornea and donor lenticule obtained algorithmically and manually (average of four manual estimates). Notation: SD–Standard deviation.

Region	Location	Parameter	Unit	Algorithmic	Manual (Average)
Recipient Cornea	Central	Min–Max	μm	371.55–963.30	378.44–1004.58
		Mean \pm SD	$\mu\text{m} \pm \mu\text{m}$	548.24 ± 112.09	560.59 ± 121.04
	Left peripheral	Min–Max	μm	371.55–963.30	364.67–997.70
		Mean \pm SD	$\mu\text{m} \pm \mu\text{m}$	560.53 ± 112.17	567.84 ± 117.80
	Right peripheral	Min–Max	μm	371.55–935.77	371.55–970.18
		Mean \pm SD	$\mu\text{m} \pm \mu\text{m}$	566.67 ± 114.27	570.05 ± 118.43
Donor Lenticule	Central	Min–Max	μm	55.04–564.22	55.04–502.04
		Mean \pm SD	$\mu\text{m} \pm \mu\text{m}$	256.92 ± 98.34	284.01 ± 102.96
	Left peripheral	Min–Max	μm	41.28–467.88	75.68–509.17
		Mean \pm SD	$\mu\text{m} \pm \mu\text{m}$	263.18 ± 95.98	290.15 ± 101.22
	Right peripheral	Min–Max	μm	68.80–660.55	68.80–681.19
		Mean \pm SD	$\mu\text{m} \pm \mu\text{m}$	266.92 ± 104.09	293.96 ± 114.54

addition, anecdotal evidence favors thinner grafts to lessen DSAEK induced hyperopic shift. Against this backdrop, endothelial keratoplasty surgeons seek the ideal DSAEK graft thickness that would lead to high visual acuity, low complication rate, and the least adverse effect on IOP. Consequently, determination of corneal thickness at different locations assumes clinical significance.

Accordingly, we algorithmically measured thickness of recipient cornea and donor lenticule at three locations, namely, at central location of the recipient cornea and at peripheral locations 1626.09 μm left and right of the central location. In particular, these estimates are calculated along the inward normals at the respective locations of the recipient cornea (see Fig. 3.11). In the 27 eyes under consideration, mean thickness values of the host cornea at central and the two peripheral locations were observed to be $548.24 \pm 112.09\mu\text{m}$, $560.53 \pm 112.17 \mu\text{m}$ and $566.67 \pm 114.27 \mu\text{m}$, which are close to the corresponding manual estimates of $560.59 \pm 121.04 \mu\text{m}$, $567.84 \pm 117.80 \mu\text{m}$ and $570.05 \pm 118.43 \mu\text{m}$, respectively. Similarly, the mean and the standard deviation of thickness of the donor graft were algorithmically obtained as $256.92 \pm 98.34 \mu\text{m}$, $263.18 \pm 95.98 \mu\text{m}$ and $266.92 \pm 104.09 \mu\text{m}$, respectively, vis-à-vis corresponding manual estimates of $284.01 \pm 102.96 \mu\text{m}$, $290.15 \pm 101.22 \mu\text{m}$ and $293.96 \pm 114.54 \mu\text{m}$, presenting satisfactory match. See Table 3.3 for further details.

Further, the correlation coefficients between manual and proposed method for thickness measurements of recipient and donor cornea, measured at central and two

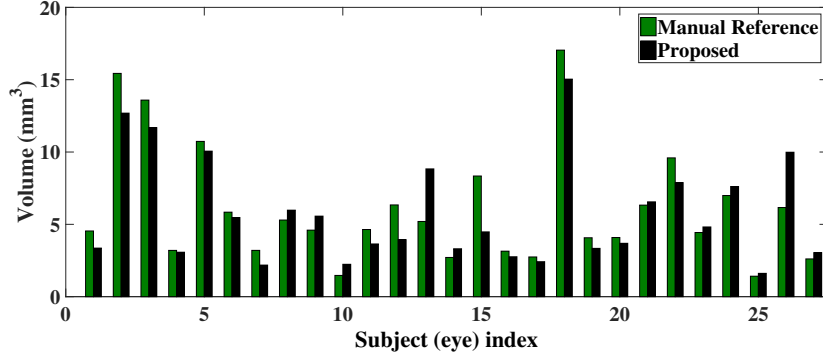


Figure 3.12: Volume estimates of detachment obtained by proposed and manual methods (manual method here indicates average of volumes estimate by all four observer delineations).

Table 3.4: Comparison of volume estimates of detachment region obtained by the proposed and manual methods. Notation: M^A – Average of two manual segmentations performed by observer A; M^B – Average of two manual segmentations performed by observer B; M –Average of M^A and M^B .

	Method	Parameter	Unit	Value
Volume of detachment (V)	Proposed (P)	Min–Max	mm^3	1.61–15.04
		Mean (SD)	mm^3 (mm^3)	5.75 (3.58)
	M^A	Min–Max	mm^3	1.54–17.43
		Mean (SD)	mm^3 (mm^3)	6.32 (4.14)
	M^B	Min–Max	mm^3	1.29–16.66
		Mean (SD)	mm^3 (mm^3)	5.81 (3.95)
	M	Min–Max	mm^3	1.41–17.04
		Mean (SD)	mm^3 (mm^3)	6.07 (4.05)

peripheral locations was observed to be 99.90% and 99.12% (central); 99.66% and 98.39% (peripheral location left to cornea center); 99.61% and 97.84% (peripheral location right to cornea center), respectively, demonstrating the efficacy of the algorithm.

3.3.2 Volume estimates and overall thickness profile

As mentioned earlier, forming an overall clinical opinion on corneal detachment based on only four scans is difficult and prone to error. Clearly, the technological capability to represent the 3D topology should assist the clinician in this situation. In this context, we mapped the detachment as well as the corneal regions in 3D, and the volume of the detachment region is obtained. Note that the same mapping/interpolation methodology is applied to manual segmentations as well to obtain volume estimates.

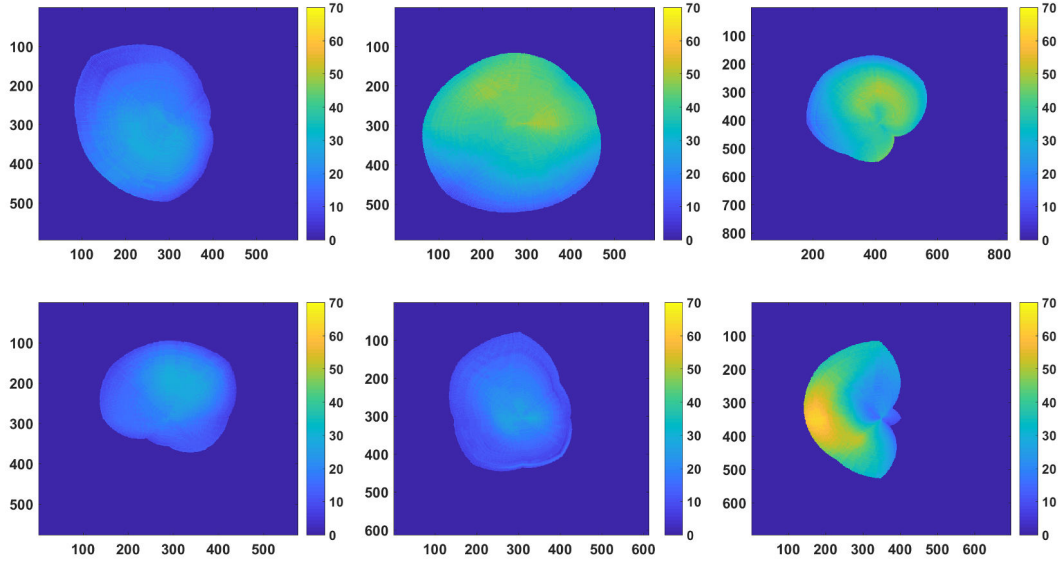


Figure 3.13: Thickness profile of the detachment for the representative images shown in Fig. 3.9. Note: Scale is shown in μm .

As presented in Table 3.4, for our dataset the algorithmic volume estimate ranges between 1.61mm^3 and 15.04mm^3 with a mean 5.75mm^3 and standard deviation 3.58mm^3 , which is in close agreement with the corresponding reference manual estimates (averaged over four independent estimates made by two different observers) ranging between 1.41mm^3 and 17.04mm^3 with a mean of 6.07mm^3 and standard deviation 4.05mm^3 , respectively. Such volume estimates are compared for each eye in Fig. 3.12, and satisfactory match is observed for most eyes with only two exceptions. In particular, the mean and standard deviation of volume estimates obtained by the proposed method are in close agreement with respective estimates obtained by manual methods, indicating the robustness of the algorithm. Indeed, volume estimates obtained by each grader are also in general agreement with the algorithmic measurements, as seen in Table 3.4.

Further, the correlation coefficients between volume measurements of detachments obtained from manual and proposed methods was observed to be 97.43% depicting the robustness of the proposed method.

Finally, detachment profile projected on to a plane normal to the corneal axis are also obtained. Detachment profiles of the six representative subjects considered earlier (see Fig. 3.9) are depicted in Fig 3.13. These profiles provide a better understanding of topology and thickness profile of the detachments.

3.4 Discussion

In this chapter, we proposed an automated methodology for 3D visualization and quantification of donor lenticule detachment post DSAEK using anterior segment OCT images. In particular, viewing the detachment in 2D as a tubular structure, we employed Hessian matrix analysis to detect it. Subsequently, to model such detachment in 3D, we employed a two stage interpolation to obtain the intermediate scans. The accuracy of the proposed method was found to compare well with observer repeatability in statistical terms. Further, quotient measures were also computed to facilitate possible comparison with future methods [38].

In anterior segment OCT images, various structures such as cornea and iris possess intensity profiles similar to that of the desired detachment, thus posing significant challenge in segmentation. Consequently, we observed that various common thresholding methods including Otsu and NiBlack methods fail to produce the optimal threshold required for segmenting corneal as well as detachment regions. In view of this, we employed more involved techniques including Yen's thresholding, Hessian matrix analysis and maximum entropy thresholding which are robust to heterogeneity in the intensity profiles of corneal and detachment regions.

While DSAEK has been a successful procedure and adopted worldwide in a short span of time, it still encountered complications such as graft detachment. In such instances, the crucial decision whether to proceed to rebubbling or to continue observation could be made with accuracy with improved visualization and quantification tools as opposed to traditional subjective examination using slit-lamp microscopy. In this context, we believe that the proposed 3D visualization and the estimated 360° detachment profile do mark a step forward in providing improved understanding of the nature of the detachment. Visante AS-OCT (time domain OCT (TD-OCT), used in the current work) is the first generation AS-OCT device which could provide wide field quad scans (radial). Complete corneal cross-section can be viewed using this device. To the best of our knowledge so far there was no advancement in terms of increase in number of radial scans acquired. The recent AS-OCT devices such as Optovue Avanti (spectral domain OCT (SD-OCT)) provides volume scans but in a limited field-of-view (for Optovue Avanti scan area is only 4mm x 6mm) not covering complete cornea [39]. In this backdrop, we believe that the currently available Visante AS-OCT quad scan is the only way to view complete cornea as well as graft detachment post DSAEK in 3D. However, our methodology does not impose any numerical restrictions on radial scans. Indeed, we plan to test the algorithm for varied number

of scans, and examine the relation between such number and the estimated volume of the detachment.

Notice that the proposed 3D interpolation assumes no holes in the recipient and donor corneal regions. Based on available image data, the above assumption appears to be reasonable. If, in certain instance, holes do exist, then the proposed algorithm would not apply in its current form, and require modification.

While the present work is a proof of concept demonstrated using limited number of subjects, in future we plan to validate the algorithm on more subjects and hence accurately determine the condition for surgical intervention. Further, it would enable clinicians to measure (and possibly predict) the progression of the detachment. At the same time, we also plan to study the effect of the detachment on visual acuity. Finally, we envision that proposed algorithm to be deployed in intraoperative OCT to enable the real time quantitative assessment of the graft detachment.

Appendix

3.A Yen's Thresholding

Yen's automated thresholding obtains the threshold based on maximum correlation criteria [30, 31]. Consider an image having N gray levels, let p_i be the probability of i^{th} gray level. For the given gray level s , if $P(s) = \sum_{i=1}^{s-1} p_i$ is larger than zero and smaller than one, then the following two distributions can be derived from this distribution after normalization.

$$A = \left\{ \frac{p_0}{P(s)}, \frac{p_1}{P(s)}, \dots, \frac{p_{s-1}}{P(s)} \right\}, \quad (3.A.1)$$

$$B = \left\{ \frac{p_s}{1-P(s)}, \frac{p_{s+1}}{1-P(s)}, \dots, \frac{p_{N-1}}{1-P(s)} \right\}. \quad (3.A.2)$$

The correlation of probability distributions A and B of an intensity level s defined as

$$C_A(s) = -\ln \sum_{i=1}^{s-1} \left(\frac{p_i}{P(s)} \right)^2, \quad (3.A.3)$$

$$C_B(s) = -\ln \sum_{i=s}^N \left(\frac{p_i}{1-P(s)} \right)^2. \quad (3.A.4)$$

Then the total correlation TC provided by the distributions A and B , is given by

$$TC(s) = C_A(s) + C_B(s). \quad (3.A.5)$$

Now, for the binarization of an image, the intensity level (s) at which the total correlation is maximized is considered as the threshold.

3.B Circle fitting

Let $(x(i), y(i))$ be the i^{th} top edge pixel and the center (x_c, y_c) and radius R of the circle is given in [32] as

$$\begin{aligned} x_c &= (c_1 b_2 - c_2 b_1) / (a_1 b_2 - a_2 b_1) \\ y_c &= (a_1 c_2 - a_2 c_1) / (a_1 b_2 - a_2 b_1) \\ R &= \left\{ \left[\sum_{i=1}^N x(i)^2 + \sum_{i=1}^N y(i)^2 + N(x_c^2 + y_c^2) - 2(x_c \sum_{i=1}^N x(i) + y_c \sum_{i=1}^N y(i)) \right] / N \right\}^{1/2}, \end{aligned}$$

where

$$\begin{aligned} a_1 &= 2 \left(\left(\sum_{i=1}^N x(i) \right)^2 - N \sum_{i=1}^N x(i)^2 \right) \\ a_2 &= 2 \left(\sum_{i=1}^N x(i) \sum_{i=1}^N y(i) - N \sum_{i=1}^N x(i)y(i) \right) \\ b_1 &= 2 \left(\sum_{i=1}^N x(i) \sum_{i=1}^N y(i) - N \sum_{i=1}^N x(i)y(i) \right) \\ b_2 &= 2 \left(\left(\sum_{i=1}^N y(i) \right)^2 - N \sum_{i=1}^N y(i)^2 \right) \\ c_1 &= \sum_{i=1}^N x(i) \left(\sum_{i=1}^N x(i)^2 + \sum_{i=1}^N y(i)^2 - N \left(\sum_{i=1}^N x(i)^3 + \sum_{i=1}^N x(i)y(i)^2 \right) \right) \\ c_2 &= \sum_{i=1}^N y(i) \left(\sum_{i=1}^N x(i)^2 + \sum_{i=1}^N y(i)^2 \right) - N \left(\sum_{i=1}^N y(i)^3 + \sum_{i=1}^N x(i)^2 y(i) \right). \end{aligned}$$

3.C Hessian matrix analysis

For each pixel (x,y) of a 2D image with intensity $I(x,y)$, the Hessian matrix ($H(x,y)$) is given by

$$H(x, y) = \begin{bmatrix} \frac{\partial^2 I(x,y)}{\partial x^2} & \frac{\partial^2 I(x,y)}{\partial x \partial y} \\ \frac{\partial^2 I(x,y)}{\partial x \partial y} & \frac{\partial^2 I(x,y)}{\partial y^2} \end{bmatrix} \quad (3.C.6)$$

Where $\frac{\partial}{\partial x}$ and $\frac{\partial}{\partial y}$ are the partial derivatives along x and y directions respectively. Sobel operator, Roberts operator and Prewitt operator are few examples of the partial differential operators. λ_1, λ_2 be the two Eigen values of $H(x, y)$ at (x, y) such that $|\lambda_1| \geq |\lambda_2|$. The filter is given as

$$V(x, y) = \begin{cases} 0 & \text{if } \lambda_1 > 0 \\ \exp(-\frac{R_\beta^2}{2\beta^2})(1 - \exp(-\frac{S}{2c^2})) & \text{otherwise.} \end{cases} \quad (3.C.7)$$

Where $R_\beta = \lambda_1/\lambda_2$ is the blobness measure in 2D, this ratio accounts for the deviation from a blob-like structure, while $S = |H| = (\lambda_1^2 + \lambda_2^2)^{1/2}$ is the second order structure-ness, this measure will be low in the background where no structure is present and the eigenvalues are small for the lack of contrast and in regions with high contrast compared to the background, the norm will become larger since at least one of the eigenvalues will be large. Here β and c are thresholds which control the sensitivity of the line filter to the measures, which can be experimentally chosen for specific applications.

3.D Max Entropy Criteria Thresholding

In the maximum entropy criterion, the basic idea is to choose the threshold such that the total amount of information provided by the object and background is maximized. Since the information is measured by entropy, the total amount of information provided by A and B is $E_A(s) + E_B(s)$, where $E_A(s)$ and $E_B(s)$, respective entropies corresponding to distributions A and B of gray level s , are defined by

$$E_A(s) = - \sum_{i=1}^{s-1} \left(\frac{p_i}{P(s)} \right) \ln \left(\frac{p_i}{P(s)} \right) \quad (3.D.8)$$

$$E_B(s) = - \sum_{i=s}^N \left(\frac{p_i}{1 - P(s)} \right) \ln \left(\frac{p_i}{1 - P(s)} \right) \quad (3.D.9)$$

Now, binarize the image, using the intensity level (s) which gives the maximum information as threshold.

Chapter 4

Anterior Chamber Depth Analysis

Accurate and automated detection of the anterior chamber depth is having lot of clinical applications. This study is used for the automated detection of the anterior chamber depth of the eye at 7 different positions (one central and 6 peripherals positions) using Rotating Scheimpflug Imaging (Pentacam) system. As anterior chamber depth is the distance from endothelium layer of Cornea to the anterior capsule of the crystalline Lens and Iris. Detection and segmentation of anterior chamber parts (Cornea, Iris and Lens) will be the consider basis for the depth extraction. By segmenting the image, depth is extracted at different locations and which even extended for 3D anterior chamber formation.

4.1 Introduction

Anterior chamber depth is an established anterior segment biometric parameter. Anatomically, it represents the distance between the Corneal endothelium and the anterior capsule of the crystalline Lens and Iris[40]. Detection of the anterior chamber depth play an important role in detection of diseases. it is also an important data point for advanced intraocular lens power calculations formulas like Haigis, Holladay-2 and Olsen.

A small anterior chamber depth may indicate zonular instability in eyes with pseudoexfoliation syndrome and should alert the cataract surgeon to the possibility of intraoperative complications[41]. Anterior chamber depth is one among the factors which determine the degree of the myopia [42]. When it is small, surgeons must also anticipate an increased risk of corneal endothelial injury during routine cataract extraction and high risk of angle closure glaucoma. Similarly, safe implantation of phakic intraocular lenses requires adequate value of depth. A very deep

anterior chamber is most oftenly seen in large myopic eyes with long axial lengths. Clinically, it carries preoperative importance for intraocular surgery. For example, cataract surgeons rely on biometric intraocular lens (IOL) power formulas, the latest generations of which increasingly respect the role of preoperative anterior chamber depth measurement[43].

In most of the studies, the authors wanted to check the usability of Rotating Scheimpflug Imaging system (Pentacam) in the anterior chamber depth calculation, where they used manual segmentation for checking whether obtained results are within clinically acceptable levels or not[44,45]. Manual detection may lead to unacceptably large subjective variations in medical decisions. The problem could amplify when it comes to monitoring the evolution of such separation with time, especially, if multiple physicians are involved. As a remedy, clinicians seek to objectively quantify anterior chamber depth.

In the current work, images from Pentacam camera (Scheimpflug imaging system) are used. When compared to ultrasonic imaging technique which are contact in nature i.e. immersion of eye in liquid is required, optical imaging methods are preferred because it is demonstrated that more repeatability of anterior chamber depth values and also has the advantages of a non-contact nature[46]. It is also found that the anterior chamber depth values obtained by the optical imaging systems like Orbscan and Pentacam are within clinically acceptable levels[44]. Even for phakic and pseudophakic eyes, the results of Pentacam are better ultrasound devices[47] .

This study is used for the automated detection of the anterior chamber depth of the eye at 7 different positions (one central and 6 peripherals positions) using Rotating Scheimpflug Imaging (Pentacam) system images. A total of 1225 anterior eye segment images of 49 patients (25 images angular images of each eye) are used. Complete automated methodology which doesn't depend on any other tools (like laser beam) for detection of the depth, it will only use the anterior eye segment image. And unlike other methods which will calculate the depth at only central location, by using this method you can calculate at any location. We can even use this system to form the 3D anterior chamber image. As anterior chamber depth is the distance from endothelium layer of Cornea to the anterior capsule of the crystalline Lens and Iris. Detection and segmentation of anterior chamber parts (Cornea, Iris and Lens) will be the consider basis for the depth extraction.

The rest of the chapter is organized as follows. Section 2 details the data acquisition and the proposed methodology. Subsequently, Section 3 presents experimental results. Finally, Section 4 concludes the work with future work.

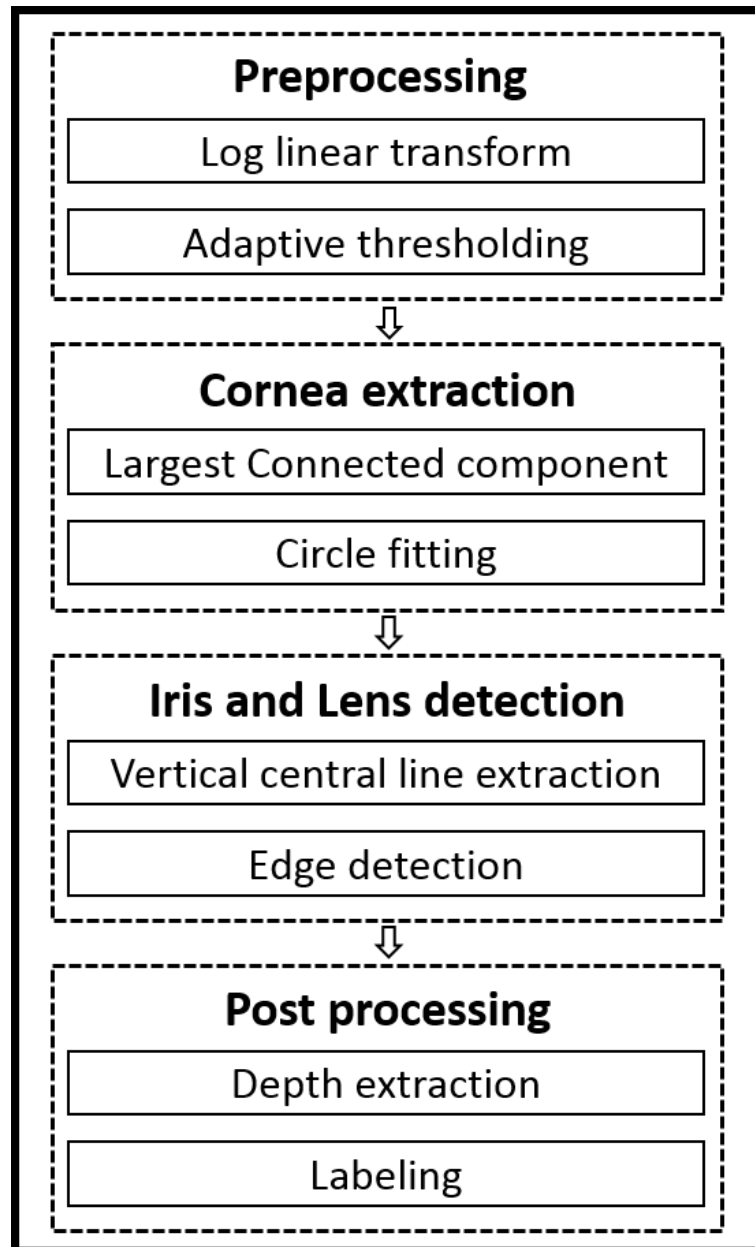


Figure 4.1: Schematic of proposed methodology.

4.2 Methods

4.2.1 Data acquisition

The present study was performed at Tej Kohli Cornea Institute, L. V. Prasad Eye Institute, Hyderabad, India. Approval from the Institutional Review Board of the institute was obtained and the subjects provided their informed consent. Further, this study was conducted in accordance with the tenets of the Declaration of Helsinki. In

particular, 49 eyes from unique patients were included in the study. On each eye, 25 Anterior segment images were obtained using Oculus Pentacam (OCULUS Optikgerte GmbH, Dublin, CA). All scans were performed by a trained optometrist.

Rotating Scheimpflug Imaging (Pentacam) was performed with the patient seated using a chinrest and forehead strap. The patient was asked to keep both eyes open and to fixate on a blinking fixation target. The system uses a rotating Scheimpflug camera and a monochromatic slit light source (blue LED at 475 nm) that rotate together around the optical axis of the eye. During 2 s, the system rotates 180 and acquires 25 images that contain 500 measurement points on the front and back corneal surface to draw a true elevation map. The software acquires the images as volume data, thus multiplanar reformations allow the creation of axial and tangential maps. Patient eye movement was constantly monitored by the system, and only measurements with less than 0.6 mm decentration were included[44].

4.2.2 Proposed Methodology

The proposed methodology is schematically depicted as a flowchart in Fig. 4.1. Major steps include (i) Preprocessing, (ii) Cornea extraction, (iii) Iris and Lens detection, and (iv) Post processing. Each of these sub steps is elaborated in the following.

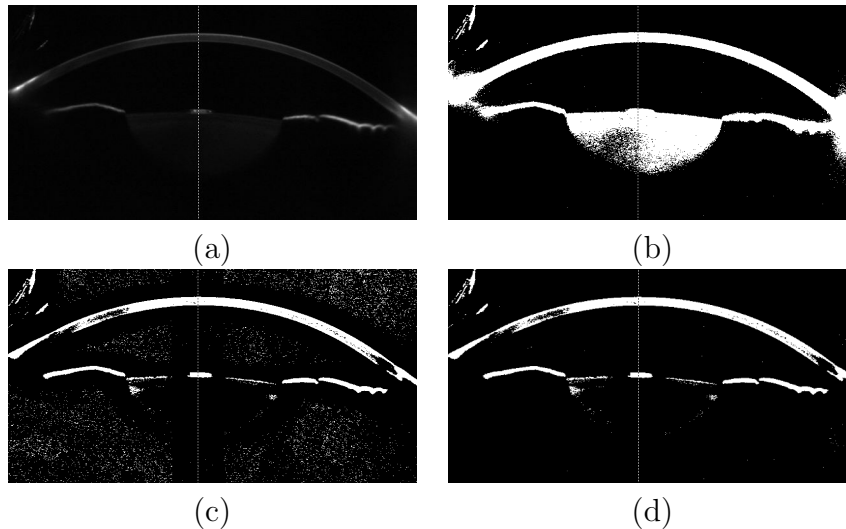


Figure 4.2: Preprocessing: (a) Pentacam anterior chamber image, (b) Log linear transformed image, (c) Adaptive thresholding image, and (d) Enhanced image.

Preprocessing:

The anterior segment images (Fig. 4.2.a) which are taken from Pentacam are generally corrupted by Speckle noise. Even intensity inhomogeneity is also one of the important factors in this imaging system, which will degrade the quality of the images. So normal edge detection techniques will fail to detect different parts like Cornea, Iris and Lens on raw images. So image enhancement will improve the quality to make the segmentation easy. From the observation of the dataset, the lens region has fine details at low intensity levels. So region-based binarization i.e. adaptive thresholding can be used and the resultant image is shown in figure 4.2.c. As there are fine details at low intensity levels, enhancement of low intensity levels can be performed by log-linear transformation. So log-linear transformation is applied on the image (Fig. 4.2.c). The enhanced image is obtained by applying both the above methods on the input image (Fig. 4.2.d).

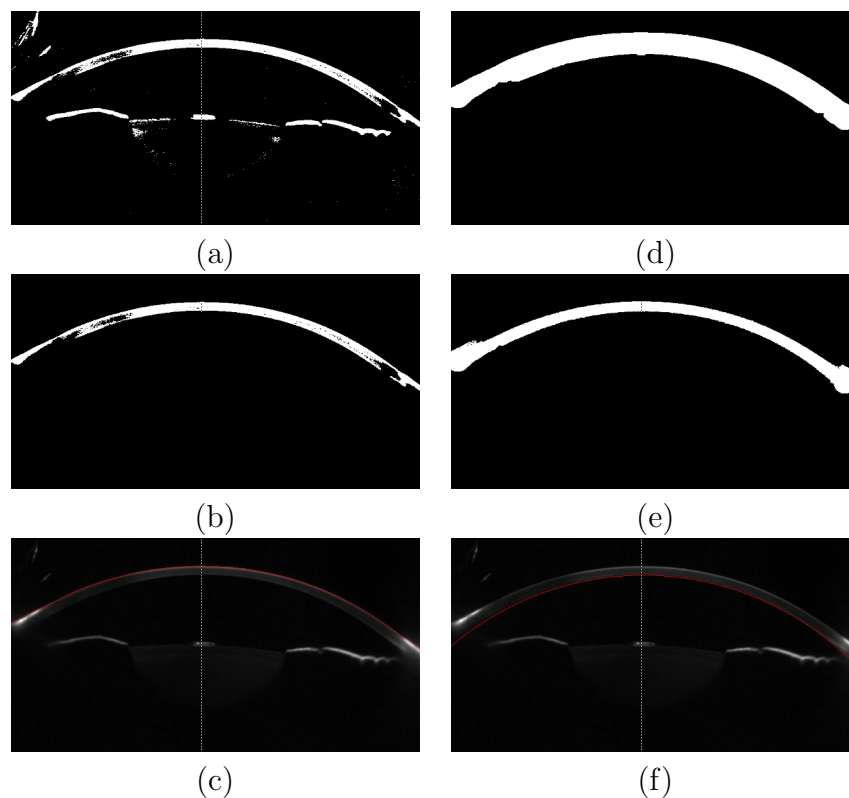


Figure 4.3: Cornea extraction : (a) Enhanced image, (b) Largest connected component, (c) Cornea outer boundary, (d) Dilate Cornea region, (e) Cornea region of Log linear transform image, and (f) Cornea inner boundary.

Cornea extraction:

The Cornea extraction involves the extraction of the Cornea inner boundary and outer boundary. Cornea is the largest among all other component in the anterior chamber so connected component is used to extract the largest connect component of the enhanced image as Cornea(Fig. 4.3.b). Its outer boundary is extracted and labeled as the Cornea outer boundary(Fig. 4.3.c). Dilate the Cornea region(Fig. 4.3.d) and multiply it with the log linear transformed image, which is nothing but extracting the Cornea region from the log linear transformed image(Fig. 4.3.e). Then extract the inner boundary of the resultant image and fit the circle to form the smooth inner boundary[32](Fig. 4.3.e).

Iris and Lens detection:

In the anterior segment images, Iris and Lens detection is the most difficult thing as the shapes of these elements are varying drastically from patient to patient. In addition to this, unexpected noisy components in images and low intensity values around the lens are making the accurate detection of Lens and Iris even difficult. The relative positioning of the Iris and Lens is the basis for detection and segmentation.

Lens, in particular to this imaging system, will touch the vertical line (dashed line). So the location of the vertical line is extracted by using the morphological operations, image close(Fig. 4.4.a) and connected components (Fig. 4.4.b). The region below the Cornea extracted(Fig. 4.4.c) and image open operation is performed(Fig. 4.4.d). The component touching the vertical line is extracted which is nothing but the Lens of the eye(Fig. 4.4.e) and its top edge is labeled(Fig. 4.4.f). As the detection of the complete Lens region from the anterior segment is difficult even manually, so we are separating the Lens and detecting only its top edge.

The region after removing the Lens and Cornea in the enhanced image is essentially the Iris. But the presence of noisy components will make the process difficult. First the Cornea, the region above the Cornea and the vertical region covered by the Lens is removed from the enhanced image(Fig. 4.5.c). Then very tiny noisy speckles and parallel components are removed by connected components(Fig. 4.5.d). Now left over components are nothing Iris. Apply canny edge detection(Fig. 4.5.e) and label the Iris edges(Fig. 4.5.f). The segment image is shown in figure 4.6.

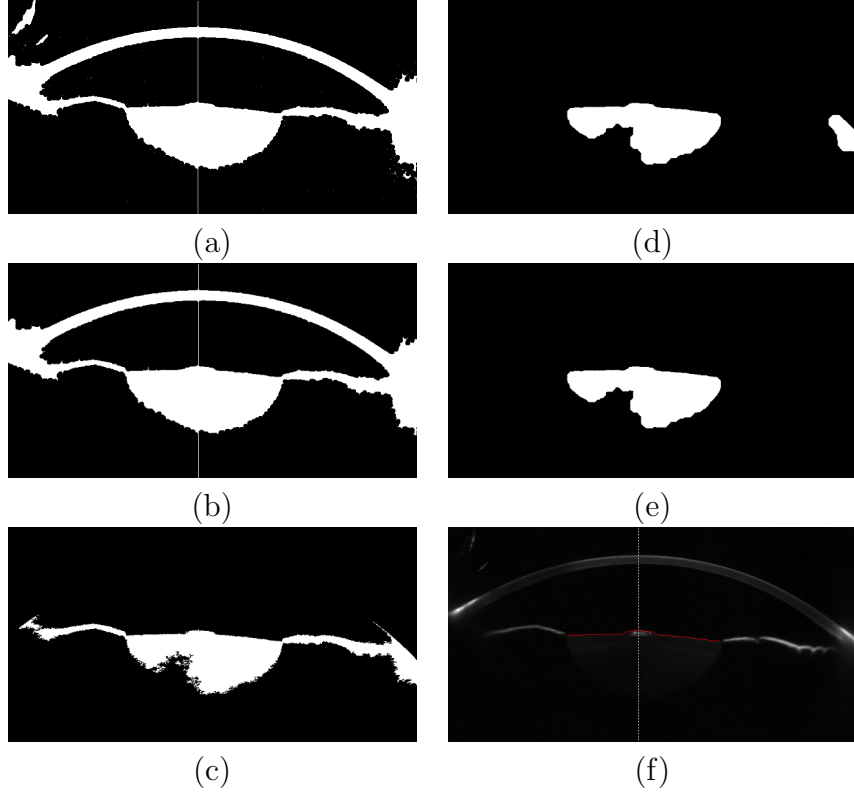


Figure 4.4: Lens extraction : (a) Image close operation Enhanced image, (b) Largest connected component, (c) The region below Cornea, (d) Image open operation, (e) component touching the vertical line, and (f) Lens top edge labeled image.

Post processing:

As the resolution of the image is $13.34 \mu\text{m} / \text{pixel}$ in horizontal direction and $21.7391 \mu\text{m} / \text{pixel}$ in vertical direction. The anterior chamber depth values at 7 different locations i.e. central and there peripheral locations on both the sides which are 1 mm apart, are calculated and labeled(Fig. 4.7).

4.3 Results

The results of the segmentation and the depth labeled images are shown in the figures 4.6 and 4.7. And the anterior chamber depth values at central location for all the datasets is shown in the graph 4.8. The average value of the anterior chamber depth at the central location is $2938.5271 \pm 260.7665 \mu\text{m}$, which is close to the ideal value 3 mm.

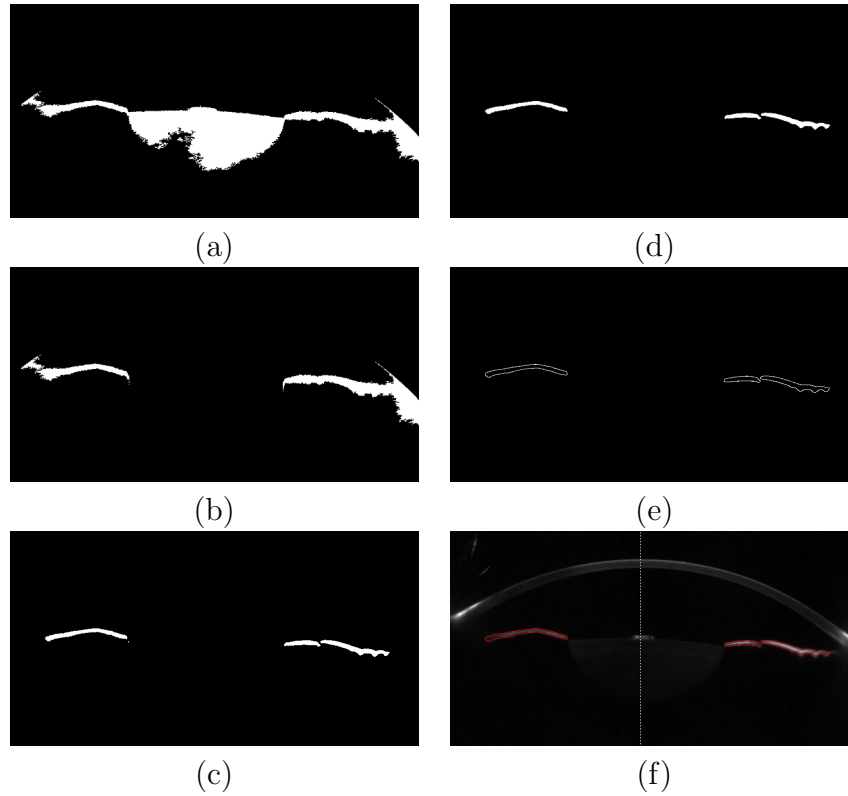


Figure 4.5: Iris extraction : (a) The region below Cornea, (b) After removing the Lens, (c) Enhanced image region, (d) After removing parallel and tiny components, (e) Canny edge detection, and (f) Iris labeled image.

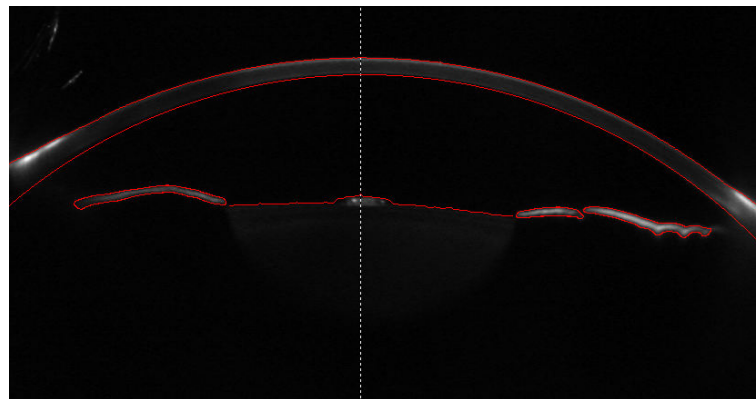


Figure 4.6: Segmentation result.

4.4 Conclusion and Future Work

The results of anterior chamber depth values are very close to the ideal values and segmentation and depth labeled images are good. But assessment of accuracy of the algorithm has to be done with respect the manual segmentation and depth calcula-

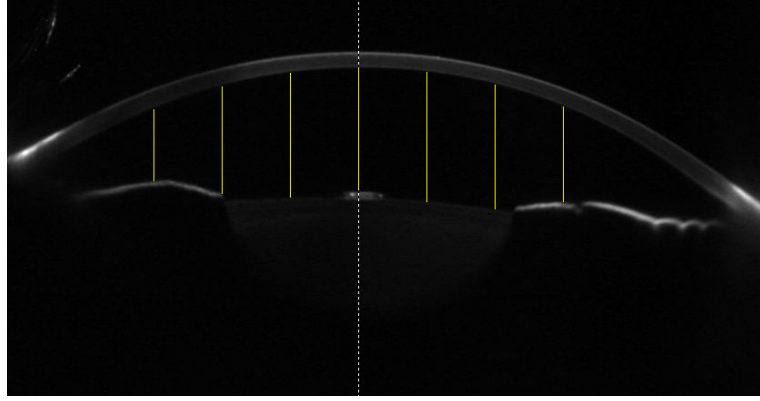


Figure 4.7: Depth labeled image.

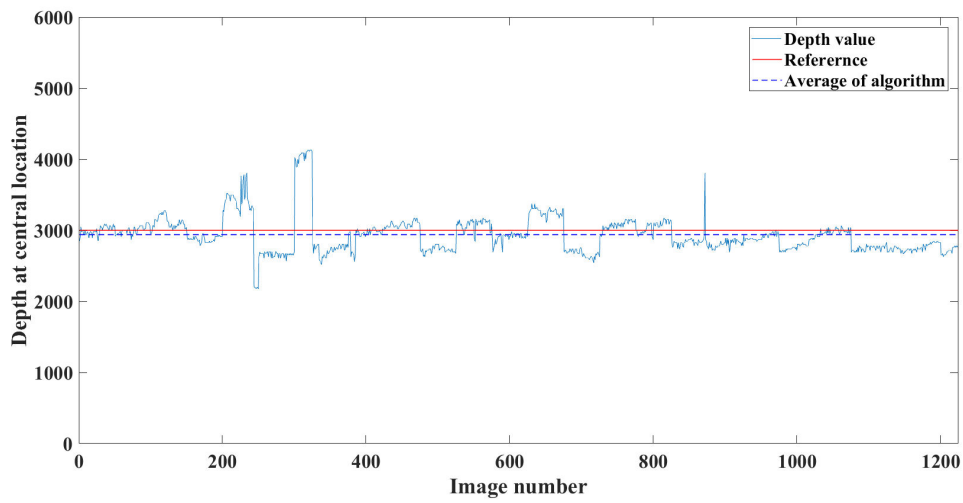


Figure 4.8: Anterior chamber depth values and comparison of average with reference.

tions. So in future, manual segmentation and depth calculations will be performed and statistical analysis like dice coefficient and correlation coefficient will be performed to check the accuracy. In addition to 2D, we can extend this for 3D anterior chamber formation by estimating and compensating the moment of the eye.

Chapter 5

Conclusion and Future Work

The designed continuous zoom slit lamp camera is having more magnification range over the existing discrete system. Part of the designed system can also be inserted into the discrete zoom system to convert it into a continuous zoom system. The real lenses model of zoom system is also having good optical parameters. In future, addition of more parameters during the optimization will make the system more realistic. This work not only helpful for the examiner to choose the region of his interest precisely but it also remove the requirement of the chin rest chamber.

The detachment of the donor lenticule from the host will form a detachment region. By using the proposed methodology in the second problem the location of the detachment in the AS-OCT and nature of detachment (communicative or non-communicative) can be detected. Complete 3D visualization of the Cornea only from 4 angular scans will help the better visualization. The obtained algorithmic values are closely following the manual values. In future, tracking the motion of the eye and the motion compensation will improve the results.

The algorithmic results of anterior chamber depth values are very close to the ideal values. And segmentation and depth labeled images are pretty close to the expected results. But assessment of accuracy of the algorithm has to be done with respect the manual segmentation and depth calculations. So in future, manual segmentation and depth calculations will be performed and statistical analysis like dice coefficient and correlation coefficient will be performed to check the accuracy. In addition to 2D, we can extend this for 3D anterior chamber formation by estimating and compensating the moment of the eye. The main take away of this method is the detection of depth values at different locations by only using the Pentacam images unlike other methods which can only detect the depth at central location using sophisticated devices.

The above described techniques in their current form or envisioned form can be

used in the diagnosis of the anterior chamber of the eye. These techniques will reduce the manual intervention, will aid the examiner to treat the patient more efficiently, remove observer variability, reduce the time requirements and electronic documentation is readily available. But the accuracy is more important than anything in the clinical domain, so the accuracy have to be improved and assessed periodically.

References

- [1] K. Tanaka, “Paraxial analysis of mechanically compensated zoom lenses. 1: Four-component type,” Applied optics, vol. 21, no. 12, pp. 2174–2183, 1982.
- [2] K. Tanaka, “Paraxial analysis of mechanically compensated zoom lenses. 2: Generalization of yamaji type v,” Applied optics, vol. 21, no. 22, pp. 4045–4053, 1982.
- [3] K. Tanaka, “Paraxial analysis of mechanically compensated zoom lenses. 3: Five-component type,” Applied optics, vol. 22, no. 4, pp. 541–553, 1983.
- [4] K. Tanaka, “Paraxial theory in optical design in terms of gaussian brackets,” PROGRESS IN OPTICS, vol. 31, pp. 63–63, 1993.
- [5] K. Yamaji, “Iv design of zoom lenses,” in Progress in optics. Elsevier, 1967, vol. 6, pp. 105–170.
- [6] M.-S. Yeh, S.-G. Shiue, and M.-H. Lu, “Two-optical-component method for designing zoom system,” Optical Engineering, vol. 34, no. 6, pp. 1826–1835, 1995.
- [7] M.-S. Yeh, S.-G. Shiue, and M.-H. Lu, “First-order analysis of a three-lens afocal zoom system,” Optical Engineering, vol. 36, no. 4, pp. 1249–1259, 1997.
- [8] R. N. Youngworth and E. I. Betensky, “Fundamental considerations for zoom lens design,” in Zoom Lenses IV, vol. 8488. International Society for Optics and Photonics, 2012, p. 848806.
- [9] W. J. Smith, Modern optical engineering. Tata McGraw-Hill Education, 1966.
- [10] M. J. Kidger, Fundamental optical design. SPIE press Bellingham, 2002, vol. 92.
- [11] J. M. Geary, Introduction to lens design: with practical ZEMAX examples. Willmann-Bell Richmond, 2002.

- [12] S. B. Koenig, D. J. Covert, W. J. Dupps Jr, and D. M. Meisler, “Visual acuity, refractive error, and endothelial cell density six months after descemet stripping and automated endothelial keratoplasty (dsaek),” Cornea, vol. 26, no. 6, pp. 670–674, 2007.
- [13] M. S. Gorovoy, “Descemet-stripping automated endothelial keratoplasty,” Cornea, vol. 25, no. 8, pp. 886–889, 2006.
- [14] M. A. Terry, N. Shamie, E. S. Chen, K. L. Hoar, and D. J. Friend, “Endothelial keratoplasty: a simplified technique to minimize graft dislocation, iatrogenic graft failure, and pupillary block,” Ophthalmology, vol. 115, no. 7, pp. 1179–1186, 2008.
- [15] W. B. Lee, D. S. Jacobs, D. C. Musch, S. C. Kaufman, W. J. Reinhart, and R. M. Shtein, “Descemet’s stripping endothelial keratoplasty: safety and outcomes: a report by the american academy of ophthalmology,” Ophthalmology, vol. 116, no. 9, pp. 1818–1830, 2009.
- [16] M. O. Price and F. W. Price Jr, “Endothelial keratoplasty—a review,” Clinical & experimental ophthalmology, vol. 38, no. 2, pp. 128–140, 2010.
- [17] F. W. Price and M. O. Price, “Descemet’s stripping with endothelial keratoplasty in 200 eyes: early challenges and techniques to enhance donor adherence,” Journal of Cataract & Refractive Surgery, vol. 32, no. 3, pp. 411–418, 2006.
- [18] S. S. Jastaneiah, “Spontaneous attachment of detached donor-corneal graft following descemets stripping automated endothelial keratoplasty,” Saudi Journal of Ophthalmology, vol. 25, no. 3, pp. 301–303, 2011.
- [19] M. Ang, M. Baskaran, R. M. Werkmeister, J. Chua, D. Schmidl, V. A. dos Santos, G. Garhöfer, J. S. Mehta, and L. Schmetterer, “Anterior segment optical coherence tomography,” Progress in retinal and eye research, 2018.
- [20] T. A. Shazly, L. K. To, I. P. Conner, and L. Espandar, “Intraoperative optical coherence tomography-assisted descemet stripping automated endothelial keratoplasty for anterior chamber fibrous ingrowth,” Cornea, vol. 36, no. 6, pp. 757–758, 2017.
- [21] V. V. Juthani, J. M. Goshe, S. K. Srivastava, and J. P. Ehlers, “The association between transient interface fluid on intraoperative oct and textural interface

- opacity following dsaek surgery in the pioneer study,” Cornea, vol. 33, no. 9, p. 887, 2014.
- [22] M. R. O’Neal and K. Polse, “In vivo assessment of mechanisms controlling corneal hydration.” Investigative ophthalmology & visual science, vol. 26, no. 6, pp. 849–856, 1985.
- [23] H. Cheng, A. K. Bates, L. Wood, and K. McPherson, “Positive correlation of corneal thickness and endothelial cell loss: serial measurements after cataract surgery,” Archives of ophthalmology, vol. 106, no. 7, pp. 920–922, 1988.
- [24] B. Holden, G. Mertz, and J. McNally, “Corneal swelling response to contact lenses worn under extended wear conditions.” Investigative ophthalmology & visual science, vol. 24, no. 2, pp. 218–226, 1983.
- [25] R.-P. Copt, R. Thomas, and A. Mermoud, “Corneal thickness in ocular hypertension, primary open-angle glaucoma, and normal tension glaucoma,” Archives of ophthalmology, vol. 117, no. 1, pp. 14–16, 1999.
- [26] J. D. Brandt, J. A. Beiser, M. O. Gordon, M. A. Kass, O. H. T. S. O. Group et al., “Central corneal thickness and measured iop response to topical ocular hypotensive medication in the ocular hypertension treatment study,” American journal of ophthalmology, vol. 138, no. 5, pp. 717–722, 2004.
- [27] K. A. Ahmed, J. W. McLaren, K. H. Baratz, L. J. Maguire, K. M. Kittleson, and S. V. Patel, “Host and graft thickness after descemet stripping endothelial keratoplasty for fuchs endothelial dystrophy,” American journal of ophthalmology, vol. 150, no. 4, pp. 490–497, 2010.
- [28] A. F. Frangi, W. J. Niessen, K. L. Vincken, and M. A. Viergever, “Multiscale vessel enhancement filtering,” in International Conference on Medical Image Computing and Computer-Assisted Intervention. Springer, 1998, pp. 130–137.
- [29] J. Schindelin, C. T. Rueden, M. C. Hiner, and K. W. Eliceiri, “The imagej ecosystem: an open platform for biomedical image analysis,” Molecular reproduction and development, vol. 82, no. 7-8, pp. 518–529, 2015.
- [30] M. Sezgin et al., “Survey over image thresholding techniques and quantitative performance evaluation,” Journal of Electronic imaging, vol. 13, no. 1, pp. 146–168, 2004.

- [31] J.-C. Yen, F.-J. Chang, and S. Chang, “A new criterion for automatic multilevel thresholding,” IEEE Transactions on Image Processing, vol. 4, no. 3, pp. 370–378, 1995.
- [32] S. M. Thomas and Y. T. Chan, “A simple approach for the estimation of circular arc center and its radius,” Computer Vision, Graphics, and Image Processing, vol. 45, no. 3, pp. 362–370, 1989.
- [33] R. C. Gonzalez, Digital image processing. Pearson Education India, 2009.
- [34] Y. Zhao, L. Rada, K. Chen, S. P. Harding, and Y. Zheng, “Automated vessel segmentation using infinite perimeter active contour model with hybrid region information with application to retinal images,” IEEE transactions on medical imaging, vol. 34, no. 9, pp. 1797–1807, 2015.
- [35] J. N. Kapur, P. K. Sahoo, and A. K. Wong, “A new method for gray-level picture thresholding using the entropy of the histogram,” Computer vision, graphics, and image processing, vol. 29, no. 3, pp. 273–285, 1985.
- [36] V. S. Gattani, K. K. Vupparaboina, A. Patil, J. Chhablani, A. Richhariya, and S. Jana, “Semi-automated quantification of retinal is/os damage in en-face oct image,” Computers in biology and medicine, vol. 69, pp. 52–60, 2016.
- [37] L. R. Dice, “Measures of the amount of ecologic association between species,” Ecology, vol. 26, no. 3, pp. 297–302, 1945.
- [38] K. K. Vupparaboina, S. Nizamapatnam, J. Chhablani, A. Richhariya, and S. Jana, “Automated estimation of choroidal thickness distribution and volume based on oct images of posterior visual section,” Computerized Medical Imaging and Graphics, vol. 46, pp. 315–327, 2015.
- [39] S. Siebelmann, U. Gehlsen, C. Le Blanc, T. P. Stanzel, C. Cursiefen, and P. Steven, “Detection of graft detachments immediately following descemet membrane endothelial keratoplasty (dmek) comparing time domain and spectral domain oct,” Graefe’s Archive for Clinical and Experimental Ophthalmology, vol. 254, no. 12, pp. 2431–2437, 2016.
- [40] M. T. Feng, M. W. Belin, R. Ambrósio, S. P. Grewal, W. Yan, M. S. Shaheen, C. McGhee, N. Maeda, T. H. Neuhann, H. B. Dick et al., “Anterior chamber depth in normal subjects by rotating scheimpflug imaging,” Saudi Journal of Ophthalmology, vol. 25, no. 3, pp. 255–259, 2011.

- [41] M. Küchle, A. Viestenz, P. Martus, A. Händel, A. Jünemann, and G. O. Naumann, “Anterior chamber depth and complications during cataract surgery in eyes with pseudoexfoliation syndrome,” American journal of ophthalmology, vol. 129, no. 3, pp. 281–285, 2000.
- [42] M. Y. Choi, I. K. Park, and Y. S. Yu, “Long term refractive outcome in eyes of preterm infants with and without retinopathy of prematurity: comparison of keratometric value, axial length, anterior chamber depth, and lens thickness,” British journal of ophthalmology, vol. 84, no. 2, pp. 138–143, 2000.
- [43] A. C. Lee, M. A. Qazi, and J. S. Pepose, “Biometry and intraocular lens power calculation,” Current opinion in ophthalmology, vol. 19, no. 1, pp. 13–17, 2008.
- [44] B. Lackner, G. Schmidinger, and C. Skorpik, “Validity and repeatability of anterior chamber depth measurements with pentacam and orbscan,” Optometry and vision science, vol. 82, no. 9, pp. 858–861, 2005.
- [45] R. S. Cauduro, C. d. A. Ferraz, M. S. A. Morales, P. N. Garcia, Y. C. Lopes, P. H. Souza, and N. Allemann, “Application of anterior segment optical coherence tomography in pediatric ophthalmology,” Journal of ophthalmology, vol. 2012, 2012.
- [46] M. Vetrugno, N. Cardascia, and L. Cardia, “Anterior chamber depth measured by two methods in myopic and hyperopic phakic iol implant,” British journal of ophthalmology, vol. 84, no. 10, pp. 1113–1116, 2000.
- [47] G. Nemeth, A. Vajas, B. Kolozsvari, A. Berta, and L. Modis, “Anterior chamber depth measurements in phakic and pseudophakic eyes: Pentacam versus ultrasound device,” Journal of Cataract & Refractive Surgery, vol. 32, no. 8, pp. 1331–1335, 2006.